



# Aerosol-deep convection interaction based on joint cell-thermal tracking in Large Eddy Simulations during the TRACER campaign

Daniel Hernandez-Deckers<sup>1</sup>, Toshihisa Matsui<sup>2,3</sup>, Takamichi Iguchi<sup>2,3</sup>, Kelcy Brunner<sup>4</sup>, Eric Bruning<sup>5</sup>, Marcus van Lier-Walqui<sup>6,7</sup>, Edward R. Mansell<sup>8</sup>, Tamanna Subba<sup>9</sup>, Chongai Kuang<sup>9</sup>, Michael P. Jensen<sup>9</sup>, and Scott Braun<sup>2</sup>

**Correspondence:** Daniel Hernandez-Deckers (dhernandezd@unal.edu.co)

Abstract. In cumulus clouds, aerosol concentrations control cloud droplet concentrations, modifying cloud radiative properties, precipitation processes, and cloud electrification. However, mechanisms of aerosol-deep convection interactions are not well understood due to complex cloud dynamics and microphysics. We investigate the interaction of aerosols with isolated deep convection using Large Eddy Simulations during the TRacking Aerosol Convection interactions ExpeRiment (TRACER) in the Houston area, using a joint cell-thermal tracking algorithm. Cumulus thermals are droplet generators, since supersaturation and droplet nucleation coincide with thermal centers, where the strongest updrafts occur. Primary ice crystal formation does not take place inside thermals, but at layers where previous thermals detrained moisture. As subsequent thermals containing supercooled droplets penetrate these layers, hail and graupel form at or near these thermals. Higher aerosol concentrations result in higher droplet concentrations that suppress drizzle, delay warm rain processes, and transport more moisture aloft. This increases snow and ice amount, as well as graupel and hail, also associated with more lightning. Also, thermals initiate slightly higher, are slightly larger and faster, suggesting a weak invigoration. We also find more thermals per cell, albeit fewer isolated cells. Convection aggregates more, explaining the lower isolated cell count, and enhancing convection, especially near the end of the 24-hour integration. This non-linear mesoscale feedback is likely triggered by temperature and moisture responses due to aerosol-thermal interactions. Additional time-lagged aerosol-reinialization experiments show that the mesoscale response is the predominant forcing for the invigoration. These changes happen within one day, on a smaller scale than previously suggested.

<sup>&</sup>lt;sup>1</sup>Departamento de Geociencias, Universidad Nacional de Colombia, Bogotá D.C., Colombia

<sup>&</sup>lt;sup>2</sup>NASA Goddard Space Flight Center Code 612, Greenbelt, MD USA

<sup>&</sup>lt;sup>3</sup>Earth System Science Interdisciplanary Center - ESSIC, University of Maryland, College Park, MD, USA

<sup>&</sup>lt;sup>4</sup>National Wind Institute, Texas Tech University, Lubbock, TX, USA

<sup>&</sup>lt;sup>5</sup>Department of Geosciences, Texas Tech University, Lubbock, TX, USA

<sup>&</sup>lt;sup>6</sup>NASA Goddard Institute for Space Studies, New York, NY, USA

<sup>&</sup>lt;sup>7</sup>Center for Climate System Research (CCSR), The Earth Institute, Columbia University, New York, NY, USA

<sup>&</sup>lt;sup>8</sup>NOAA National Severe Storms Laboratory, Norman, OK, USA

<sup>&</sup>lt;sup>9</sup>Brookhaven National Laboratory, Upton, NY, USA



20

25



## 1 Introduction

Research over the past few decades has shown that aerosols can impact the microphysics, dynamics, and electrification of clouds (Tao et al., 2012). Higher aerosol concentrations result in smaller but more numerous cloud droplets, increasing cloud albedo (Twomey, 1974), cloud cover and lifetime (Albrecht, 1989; Ackerman et al., 2000), and delaying warm precipitation processes (e.g., Andreae et al., 2004; Givati and Rosenfeld, 2004). However, when mixed-phase clouds come into play, some results suggest "invigoration" of convection due to an enhancement of vertical velocity and ice-microphysical processes (Andreae et al., 2004; Koren et al., 2005; Lin et al., 2006; Li et al., 2011; Hu et al., 2019; Abbott and Cronin, 2021; Yin et al., 2024). The former process is called warm-phase invigoration, whereas the latter process is called cold-phase invigoration (Rosenfeld et al., 2008).

The mechanisms behind these impacts are not yet fully understood. Khain et al. (2008) classified invigoration/suppression of deep convection as a function of ambient humidity associated with condensation increases/decreases due to enhanced aerosols, which highlights how different ambient conditions can lead to different responses to aerosol concentrations. Such responses are also not linear and can depend on other factors such as aerosol size. For example, using observations over the Houston area, Hu et al. (2019) found that for environments with similar Convective Available Potential Energy (CAPE), convective clouds have a higher radar echo-top height and increased lightning activity for aerosol concentrations up to 1000 cm<sup>-3</sup>. They also report that increasing aerosol concentrations above about 1200 cm<sup>-3</sup> in fact decreases lightning activity, and that differences between urban and rural areas are only present at low aerosol concentrations (less than 500 cm<sup>-3</sup>). More recently, Yin et al. (2024) show that fine aerosols invigorate deep convective systems by making them deeper and longer lived, whereas coarse sea salt aerosols inhibit convective vertical growth, but enhance warm rain production. On the other hand, convective invigoration is still debated in terms of warm- and cold-phase microphysics processes (Varble et al., 2023; Öktem et al., 2023; Fan et al., 2025). This is primarily due to the lack of fundamental understanding of the cloud microphysics associated with cloud turbulence/dynamics within the convective core, and also their dynamical feedback at different spatio-temporal scales (Hirt et al., 2020; Stephens et al., 2024).

It is widely accepted that cumulus clouds consist of updrafts that are transient in nature and actually resemble rising bubbles (e.g. Scorer and Ludlam, 1953; Saunders, 1961; Blyth et al., 2005; Sherwood et al., 2013; Yano, 2014; Romps et al., 2021). These bubbles, or "thermals", are coherent volumes of rising air, typically with an internal toroidal circulation, as shown by observations (e.g. Damiani et al., 2006) and high-resolution simulations (e.g. Hernandez-Deckers and Sherwood, 2016; Peters et al., 2020). Although conceptual models of such clouds for numerical simulations where they are not explicitly resolved have mainly been developed assuming a "steady, entraining plume" (e.g. Arakawa and Schubert, 1974), there has been a growing interest in introducing the thermal concept to better describe cumulus clouds and possibly improve cumulus parameterizations. Sherwood et al. (2013) proposed that the internal circulation within thermals could explain how high entrainment rates do not necessarily imply substantial drag, a conclusion that is not necessarily consistent with the classical steady entraining-plume concept. Romps and Charn (2015) showed that, nevertheless, thermals do sustain significant drag that balances buoyancy, so that they rise at nearly constant speed. Hernandez-Deckers and Sherwood (2016) performed a more detailed momentum budget



70



analysis, which highlighted the transient nature of thermals, and Hernandez-Deckers and Sherwood (2018) tested multiple entrainment relations for thermals, finding that thermal size is the most relevant determining factor, but it explains only 20% of total variance. Other studies have further investigated thermals and their properties within clouds, with a particular interest in the development of new cumulus parameterizations (e.g. Morrison and Peters, 2018; Morrison et al., 2020a; Peters et al., 2020; Romps et al., 2021; Gu et al., 2020; Morrison et al., 2023; Stanford et al., 2025).

Recent research increasingly utilizes thermals as a fundamental reference frame for investigating convective microphysical processes within numerical simulations. For instance, Hernandez-Deckers et al. (2022), hereafter HD22, emphasized the critical role of thermals as "cloud droplet/raindrop producers", demonstrating that the formation of cloud droplets and their subsequent growth into raindrops are strongly governed by internal thermal circulations, supersaturation levels, and cloud nucleation processes. Sampling convective regions through the reference of thermals has proven to be a more effective approach for examining microphysical processes and their sensitivity to background aerosol number concentrations compared to methods relying solely on grid point selection based on specific thresholds.

Furthermore, Matsui et al. (2024), hereafter MA24, utilizing thermal tracking to analyze simulated dry- and wet-season deep convection over the Amazon, demonstrated a distinct role for thermals in cold-phase microphysics. Their findings indicated that ice and snow crystals predominantly form outside of thermals, specifically in regions where prior thermals have detrained cloud droplets. Subsequently, when droplet-laden thermals ascend into this ice-rich layer, riming processes are enhanced, leading to the production of graupel and hail embryos within the thermal cores. These two studies collectively highlight the importance of thermals and their ensembles as a crucial framework for understanding the development of convective microphysics within moist deep convection, influenced by both background aerosols and thermodynamic environments.

This study investigates the impact of aerosols on the microphysics and dynamics of isolated deep convective cells using large-eddy simulations (LES) coupled with Lagrangian tracking of convective cells and thermals. The manuscript is structured as follows: Section 2.1 details the selection of sea-breeze-driven isolated deep convection events observed around the Houston Metropolitan area and the characterization of background aerosol concentrations based on seasonal in situ measurements. Section 2.2 describes the LES model configuration, which incorporates a sophisticated double-moment microphysics scheme with an explicit representation of electric charging and discharging processes. A novel joint cell-thermal-tracking algorithm, developed for this study and applied to the high spatiotemporal resolution LES output, is presented in Section 2.3. Section 3 will present the results of these analyses, aiming to disentangle the complex interactions between microphysics, dynamics, and electrification within simulated isolated deep convection as a function of background aerosol concentrations. Furthermore, the intricate feedback mechanisms associated with cumulus thermals will be examined and discussed. Finally, Section 4 provides a summary of the findings, a discussion of potential uncertainties, and an outline of future research directions.



110



## 2 Data and Methods

## 2.1 TRACER campaign

The US Department of Energy (DOE) Atmospheric Radiation Measurement (ARM) program's TRacking Aerosol Convection interactions ExpeRiment (TRACER) took place between October 2021 and September 2022 in the region in and around Houston, TX, with the goal of observing thunderstorms in the region together with their aerosol and thermodynamic environments (Jensen et al., 2025). The first ARM Mobile Facility (AMF1) captured a full suite of surface meteorological conditions, released frequent sounding balloons, and included detailed radiometric measurements. High-resolution scanning polarimetric radars characterized storm lifecycle, while surface-based, boat, and drone-borne instrumentation sampled aerosol and thermodynamic conditions in the boundary layer. Additional detection antennas were used to augment the Houston Lightning Mapping Array (HLMA), improving coverage and accuracy of lightning flash detection (Bruning et al., 2024). Observations were emphasized during an Intensive Observing Period (IOP) from 1 June to 30 September, 2022 when thunderstorm cells were automatically tracked, additional sondes were released, and guest instrumentation was brought to bear on environmental and aerosol sampling.

Aerosol size distributions were derived from Scanning Mobility Particle Sizer (SMPS) observations (Singh and Kuang, 2024) at the AMF1 site, during the TRACER field campaign (Jensen et al., 2022, 2025). The SMPS is a part of the operating Aerosol Observing Systems (AOS), which serves as the primary ground-based platform for in situ aerosol measurements (Uin et al., 2019). The SMPS measures aerosol size distribution (dN/dlogDp) for particle diameters (Dp) ranging from 10 to 500 nanometers (nm). The dN/dlogDp values were integrated across different size bins to calculate the total aerosol number concentration.

Two aerosol regimes are considered, representing clean and polluted conditions, based on measurements taken from 17 June to 7 August 2022. The clean regime is defined by samples with the total aerosol concentration below the 10th percentile. The polluted regime includes samples with concentrations above the 90th percentile. The aerosol modal representation presented here is based on a combination of qualitative assessment and closure of total number concentration between the observations and the best fit modes. Following Seinfeld and Pandis (2006), the aerosol size distributions were approximated using a sum of up to three lognormal functions, individually representing nucleation, Aitken, and accumulation modes. The parameters, including number concentration (Na), median diameter (Dm), and the standard deviation (Sigma) for the modal distributions, are shown in Table 1 for clean and polluted regimes. These values are homogeneously initialized within the regional LES.

Note that there are several approaches to distinguishing clean and polluted conditions, such as separating continental and maritime regimes (Matsui et al., 2020a; Iguchi et al., 2020) or employing more gradual classifications rather than focusing solely on extreme values (Hernandez-Deckers et al., 2022). In this study, however, we adopt a more fundamental separation to examine the model's behavior in simulating aerosol impacts on sea-breeze-driven isolated deep convection.





**Table 1.** Lognormal aerosol modal parameters derived from SMPS observations for clean and polluted cases: Number concentration (Na), median diameter (Dm) and standard deviation (Sigma).

Aerosol properties	Mode 1 (Nucleation)	Mode 2 (Aitken)	Mode 3 (Accumulation)
Na (clean) (cm <sup>-3</sup> )	352	391	260
Na (polluted) (cm <sup>-3</sup> )	11518	3462	454
Dm (clean) (nm)	17	54	165
Dm (polluted) (nm)	20	51	167
Sigma (clean)	1.6	1.5	1.4
Sigma (polluted)	1.6	1.6	1.5

#### 2.2 NU-WRF simulations

115

120

125

130

The NASA-Unified Weather Research and Forecasting (NU-WRF; e.g. Peters-Lidard et al., 2015) model was utilized as a limited-area weather model to simulate convection, the behavior of which is analyzed by the thermal and cell tracking algorithm. NU-WRF is a superset of the National Center for Atmospheric Research (NCAR) WRF Advanced Research core (ARW; Skamarock et al., 2008) with additional components developed at NASA Goddard Space Flight Center. The version of NU-WRF used here, tailored for simulating the cases of the TRACER field campaign, is denoted as NU-WRF with Electrification, a Polarimetric radar Instrumental simulator, and Cloud condensation nuclei (NU-WRF EPIC). NU-WRF EPIC is based on NU-WRF version 9 patch 3 and WRF-ARW version 3.9.1.1.

Three nested simulation domains, with horizontal grid spacings of 3, 1, and 0.2 km, were set up to cover an approximately 200 km x 170 km area around the Houston metropolitan area. The initial conditions for all domains, as well as the lateral boundary conditions for the outermost domain, were prepared using the ECMWF Reanalysis 5th Generation (ERA5) dataset (Hersbach et al., 2020). First, the two larger domains with grid spacings of 3 and 1 km were simulated simultaneously to produce the lateral boundary conditions for the 0.2 km domain. Then, the innermost domain was simulated at near LES scales, and the results were used for analysis. Model atmospheric columns extended from the surface up to 100 hPa and were divided into 91 layers across all domains.

The 2017 versions of the Goddard shortwave and longwave radiation schemes (Chou and Suarez, 1999; Chou et al., 2001; Matsui et al., 2020b), which do not incorporate the radiative effects of aerosols, were used to calculate the atmospheric radiation flux and heating. No planetary boundary layer (PBL) parameterization scheme was used in the simulations for LES, while the level-2.5 Mellor-Yamada-Nakanishi-Niino (MYNN) turbulence scheme (Nakanishi and Niino, 2006, 2009) was used for large-domain simulations. The physics and structure of the surface layer were parameterized based on the traditional Monin-Obukhov similarity theory (Monin and Obukhov, 1954). The community Noah land surface model with multi-parameterization (Niu





et al., 2011; Yang et al., 2011) was used to calculate land surface processes and surface heat fluxes. The Moderate Resolution Imaging Spectroradiometer (MODIS) global dataset with 21 land use categories and 30-minute horizontal resolution (e.g. Friedl et al., 2002) was used for categorizing land use and land cover. A single-layer urban canopy model (Kusaka et al., 2001; Kusaka and Kimura, 2004; Chen et al., 2011) was used to incorporate urban effects for metropolitan areas. No subgrid convection parameterization was used in any domain.

The National Severe Storms Laboratory (NSSL) two-moment bulk microphysics scheme was used to calculate grid-scale cloud microphysics. This microphysics scheme predicts the mass and number concentrations of the six hydrometeor categories (cloud water, rain, ice crystals, snow, graupel, and hail). Bulk densities are also predicted for the graupel and hail categories, allowing "graupel" to represent the range from rimed snow to frozen drops. The cloud microphysics parameterization is coupled with parameterizations for cloud electrification (Mansell et al., 2005, 2010) and bulk discharge processes (Fierro et al., 2013). Both non-inductive and inductive charging were considered, as both processes have proven important in simulating various thunderstorm modes, including thundersnow (Harkema et al., 2024).

The nucleation process of cloud water droplets from aerosol particles in NU-WRF EPIC is calculated based on the parameterization developed in Abdul-Razzak and Ghan (2000) from tri-modal size distributions, with Na specified from the SMPS observations (Section 2.1). Heterogeneous ice nucleation is based on the parameterization from DeMott et al. (2010). The Na values are initialized as horizontally homogeneous without the addition of aerosols during the simulations. The initial vertical distribution of Na is homogeneous from the ground to 1,500 meters above the mean sea level. Above that level, Na decreases with increasing height, with an 800-meter scale height. The kappa value for the aerosol particles was set at 0.12. This value was calculated from the cloud condensation nuclei (CCN) observations at the TRACER-AMF1 site (Koontz et al., 2021) and represents the average value over the deployment.

A semi-diagnostic method (Fridlind et al., 2017) was employed to track aerosol number concentrations. This approach predicts CCN concentrations at each time step for a specified supersaturation. Cloud droplet number concentration increases only when the predicted number of activated CCN exceeds the existing cloud droplet number concentration. Notably, this nucleation scheme does not explicitly account for aerosol loss; aerosol removal is only considered during the conversion of cloud droplets to raindrops.

Note that considerable uncertainties remain for the parameterization of many microphysical processes, including initial formation of rain through collision-coalescence, vapor growth of ice, and secondary ice production, among other processes (Morrison et al., 2020b). The consequences of these individual uncertainties in the aggregated and emergent behavior of a deep convective thunderstorm are complex and may be substantial, but are outside the scope of this study.

## 2.3 Lagrangian Cell and Thermal Tracking

165

The convective cells within the simulations were tracked using the open-source Tracking and Object-Based Analysis of Clouds (TOBAC) software (Heikenfeld et al., 2019; Sokolowsky et al., 2024). Storm cells were identified at each model output time step (1 minute in this study) as contiguous regions within the simulated 2D composite reflectivity field exceeding a minimum threshold of 15 dBZ (defined as a TOBAC 'feature'). The spatial extent of each feature was determined through watershed



170

175

180

185

195

200



segmentation and subsequently linked across time steps. A final processing step evaluated cell merging and splitting to refine storm cell tracks. To isolate deep convective cells, criteria based on minimum/maximum area ( $25\sim400~\text{km}^2$ ), minimum duration (>30 min), and maximum reflectivity (> 25 dBZ) throughout cell lifecycles were applied to exclude too small/large anomalous cells. Additionally, a maximum number of neighboring features was defined to exclude aggregated cells from the analysis.

Each of these cells generally comprises numerous updrafts, which often manifest as small, short-lived cumulus thermals (Blyth et al., 2005; Damiani et al., 2006; Sherwood et al., 2013; Yano, 2014). Within each identified isolated convective cell defined by TOBAC, these thermals were tracked following the methodology outlined by Hernandez-Deckers and Sherwood (2016). Specifically, subdomains of tracked isolated cells were defined at each model-output time step (1 minute); then, the thermal-tracking algorithm is applied to this subdomain that encompasses each tracked cell. While previous studies (e.g., HD22 and MA24) focused on a fixed sub-domain for the entire time period, this new technique allowed us to track thermals of multiple moving targets individually.

The thermal tracking method identifies and follows coherent, rising quasi-spherical volumes of air using the velocity, pressure, temperature, and water content fields. Initially, local maxima of vertical velocity are identified and tracked over time, and these points are considered the centers of potential rising thermals. Based on the trajectories of these centers, each thermal's center ascent rate is estimated at each output time step. A spherical radius is then determined such that the average vertical velocity within this volume matches the estimated ascent rate, providing an estimate of the thermal's size. Subsequently, the vertical momentum budget of each thermal is computed using the temperature, pressure, and water content fields, serving as a criterion to validate the correct identification of tracked thermals. Further details regarding this identification and tracking method are provided in Hernandez-Deckers and Sherwood (2016). While acknowledging that thermals are not strictly spherical, this tracking method assumes a spherical shape, which has been demonstrated to be a reasonable first-order approximation (Hernandez-Deckers and Sherwood, 2016).

Following the identification and tracking of thermals, composites are computed by averaging thermals normalized by their radius and weighted by their mass flux. This compositing can be performed for selected subsets of thermals, such as those categorized by altitude or stage of development, yielding valuable statistical insights into the microphysical and dynamical characteristics of thermals, and consequently, convection, given that thermals are the building blocks of convective cells. A similar methodology has been applied in prior research; for instance, Hernandez-Deckers and Sherwood (2018) utilized it to examine the impact of entrainment on cumulus convection, HD22 employed it to investigate warm microphysical processes within thermals, and MA24 used it to explore the dry-wet season contrast in convective mixed-phase microphysics over the Amazon. In this study, we employ this approach to investigate the response of cold- and warm-phase microphysics and electrification processes within thermals to varying aerosol loading conditions during isolated deep convective events.

## 2.4 Case selections

Prior to this study, NU-WRF EPIC simulations with horizontal grid spacings of 3 and 1 km were conducted to support the daily operations of the TRACER field campaign. The forecast performance was concurrently evaluated against the NEXRAD



210



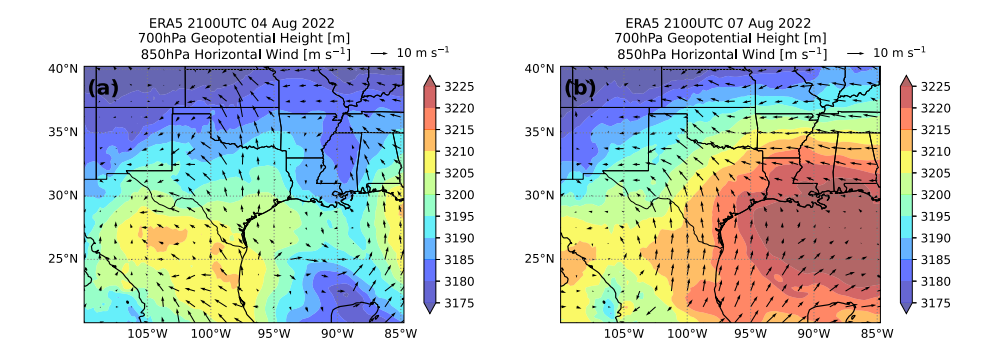


**Figure 1.** Geopotential height at the 700 hPa level and the horizontal wind at the 850 hPa level at 2100 UTC on (a) August 4 and (b) August 7, 2022, from the ERA5 reanalysis.

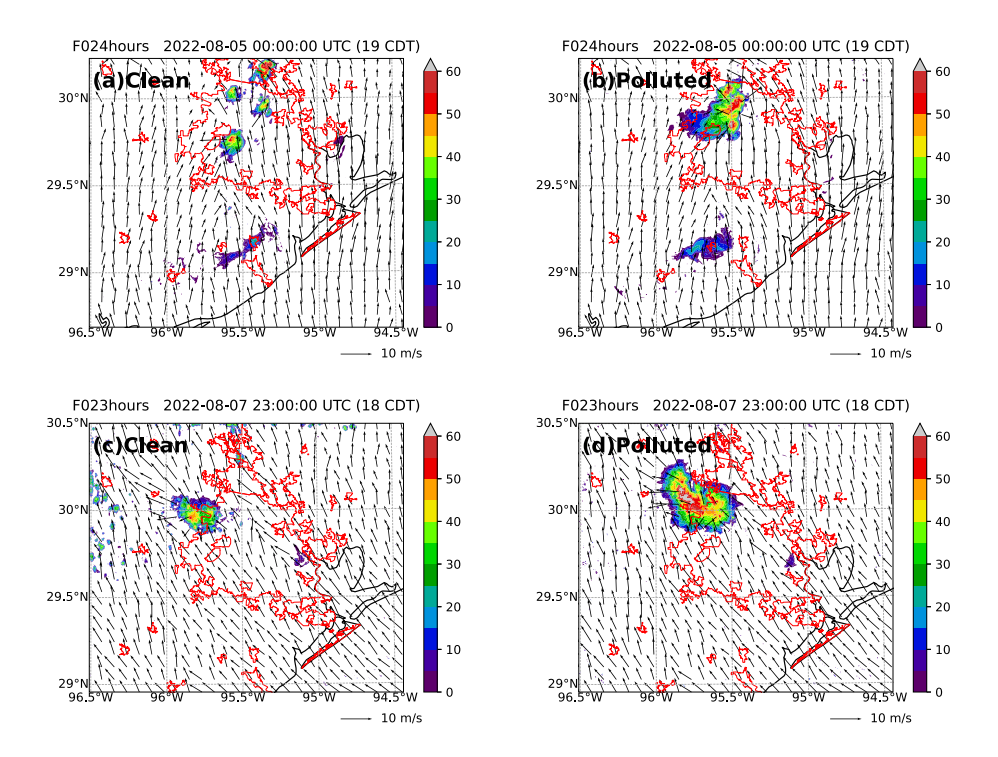
radar composite using a polarimetric radar simulator and composites (Matsui et al., 2023). Polarimetric radar-based skill scores were calculated for the daily forecasting results. TOBAC analysis was also employed to quantify the number of isolated cells during the IOP from both NEXRAD observations and NU-WRF EPIC-simulated NEXRAD signals. These comparisons (not shown here) indicated that higher model forecasting skill scores were strongly correlated with a larger number of isolated cells, suggesting that NU-WRF EPIC tends to exhibit better forecasting skill for isolated convective cases. Based on a careful investigation of these results, two representative cases were identified to investigate the aerosol impact on the cumulus thermals of isolated convective cells: 4 August and 7 August, 2022. The simulations started at 00 UTC each day.

Figure 1 illustrates the geopotential heights at 700 hPa and the horizontal winds at 850 hPa at 2100 UTC for the two cases. According to Wang et al. (2022), who conducted an analysis and classification of the summer synoptic regimes over this region at a climatological scale, the synoptic pattern on 4 August is categorized roughly as a post-trough regime. In this regime, the Houston area was located to the west of a trough, and it was dominated by a weak northerly wind developed between the eastern trough and the western ridge. In contrast, the synoptic pattern on 7 August is categorized as an anticyclonic regime, characterized by a high pressure system over the Gulf and coastal area. These are conditions conducive to the sea-breeze development and isolated convection in the afternoon, under stable and weak synoptic forcing.

Figure 2 shows the composite radar reflectivity from the LES domain at the time when convective development is near the peak in each case. At these times, convection was simulated on the northwestern side of the Houston metropolitan area. The magnitude and structure of the composite radar reflectivity are quite different for the clean/polluted aerosol cases. The subsequent section presents a detailed analysis of the characteristics of convection and cloud microphysics through Lagrangian tracking of convective cells and thermals.







**Figure 2.** Composite radar reflectivity (color field) with horizontal wind at 10 m above the ground level (black arrows) in the model simulations, overlaid with the coastline (black line) and urban-rural classification (red lines) defined by the U.S. Census Bureau for the year 2020, with (a, c) Clean and (b, d) polluted aerosol conditions.

#### 220 3 Results

225

230

# 3.1 Cumulus thermals

The TOBAC cell tracking algorithm identified and tracked 17 isolated convective cells in the 4 August clean case, 18 in the 7 August clean case, 6 in the 4 August polluted case, and 7 in the 7 August polluted case. Figure 3 illustrates the locations and evolutions of the tracked cells for the 4 August polluted case, along with time-altitude plots of mass flux for individual thermals within one of the tracked cells. Notably, most thermals exhibit relatively low mass flux (92-95% of thermals have mass flux lower than  $2 \times 10^5$  kg m s<sup>-1</sup>), as well as short lifetimes (90% of thermals live less than 9 min), and short travel distances (85-90% travel less than 2 km), consistent with prior findings (e.g., Sherwood et al., 2013; Hernandez-Deckers and Sherwood, 2016). However, a subset of thermals, initiated during the mature stage of the convective cell, displays comparatively longer lifespans (1% of thermals live 12 min or longer), greater travel distances (1% of thermals travel at least 4 km), higher final altitudes (1% of thermals reach above 10km), and larger contributions to the mass flux (1% of thermals have at least  $4 \times 10^5$  kg m s<sup>-1</sup> mass flux), likely playing a key role in mixed-phase precipitation processes (MA24). It is also important to note that clear "lucky" thermals are not captured during the deepest time of convection (1300 1340). That is, thermals that would



240

245

250

255



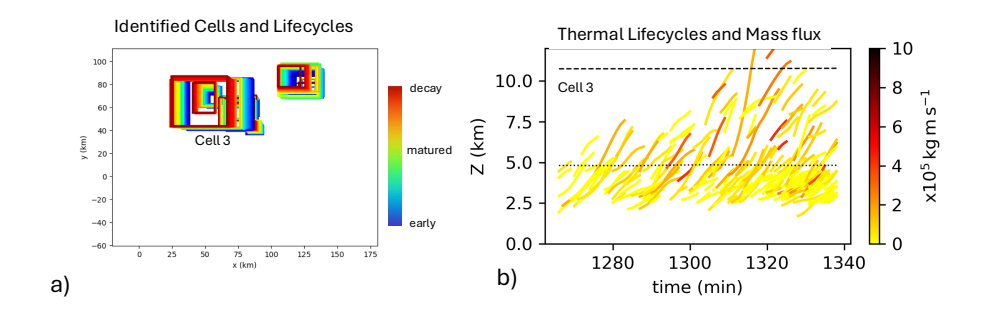


**Figure 3.** a) Isolated convective cells identified through cell tracking and their life cycles for the 7 August polluted case. Colors indicate life cycle stage while box size indicates sizes of cells. b) Time-height trajectories of tracked thermals and mass flux (color shade) from Cell 3 [the largest boxes in a)]; dashed line corresponds to the -40°C level, and the dotted line to the 0°C level.

initiate at the cloud base and ascend continuously to the cloud top, which contrasts with the common conceptualization of deep precipitating convection (e.g., Emanuel, 1994). These robust, strong thermals typically occur from the middle height of the convective cells. It is also possible that smaller shallow thermals may merge to form larger thermals, which can penetrate to the cloud top and behave as "lucky thermals". However, the potential impacts of such merging processes have not yet been investigated in this study.

The thermal tracking algorithm identified a total of 1263 thermals within the isolated cells of the clean cases (434 in the 4 August case and 829 in the 7 August case), and 561 thermals in the polluted cases (87 in the 4 August case and 474 in the 7 August case). Notice that although fewer thermals were identified in the polluted cases compared to the clean cases, there are actually more identified thermals per cell in the polluted cases (43 thermals/cell for polluted against 36 thermals/cell for clean). Furthermore, the lower number of tracked cells in the polluted cases does not necessarily indicate less overall convective activity. In fact, convection in the polluted cases tends to exhibit greater aggregation compared to the clean cases (e.g., Fig. 2), resulting in fewer identified "isolated" cells, but not necessarily less convection overall (discussed in Section 3.2). Additionally, it is worth considering that radar-based cell identification can be biased towards precipitation particles because radar reflectivity is related to the sixth moment of hydrometeor sizes. Consequently, some polluted cells may suppress precipitation, becoming less detectable by the radar reflectivity threshold used by TOBAC (Section 2.3). Hereafter, statistical composites of thermal properties integrate all tracked thermal properties from detected isolated cells of the 4 and 7 August simulations for "clean" and "polluted" cases, and their difference ("polluted-clean").

Figure 4 shows cross-sections of vertically and time averaged thermal composites. Similar to HD22 and MA24, after identifying individual thermals, the analysis centers on each thermal's peak vertical velocity (thermal maxima) as a reference point. For all cross-sections shown here, thermal properties are averaged using mass flux-based weights to emphasize stronger thermals. Note that this may result in slight differences when averaging for the entire column (Fig. 4) and when averaging at different altitudes (Figs. 7-8), since thermals reach their maxima at different heights. However, this does not affect our interpretation of results.





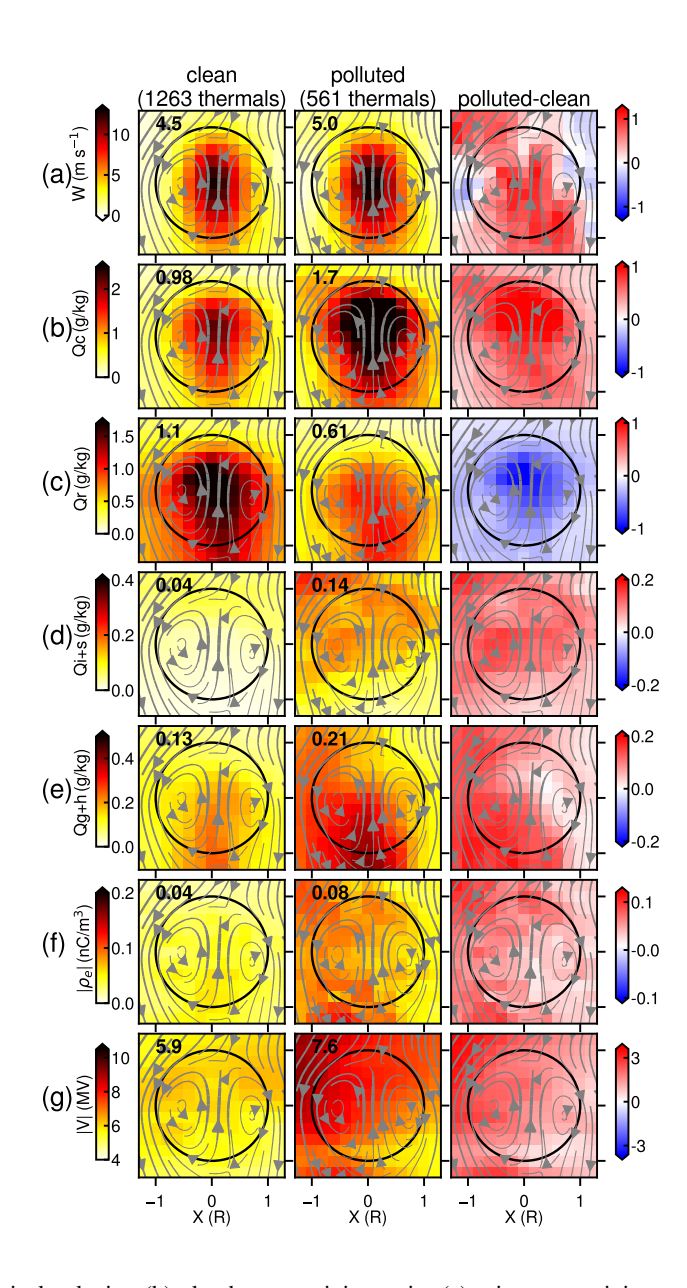


Figure 4. Composites of (a) vertical velocity, (b) cloud water mixing ratio, (c) rain water mixing ratio, (d) ice+snow mixing ratio, (e) graupel+hail mixing ratio, (f) absolute value of volume charge density and (g) absolute value of electric potential, averaged over altitude and the entire thermal lifetime for the clean cases (left column), polluted cases (middle column) and their difference (right column). The bolded values indicate the in-thermal averages of each quantity. The background wind fields shown in the third column are taken from the clean cases.

Variations in background aerosol conditions exert influence on thermal properties. Specifically, the polluted case exhibits higher cloud water mixing ratios compared to clean cases (Fig. 4b), aligning with enhanced droplet nucleation and condensa-



260

265

270

275

280

285

290



tion. This increased droplet concentration subsequently suppresses warm-rain processes in the polluted case (Fig. 4c), a finding consistent with HD22's results using a different double-moment microphysics scheme. The NU-WRF EPIC simulations show that enhanced condensation is associated with increased vertical velocities (Fig. 4a) in contrast to HD22, who did not find enhanced vertical velocities associated with enhanced condensation. This discrepancy will be discussed later.

The increased cloud droplet concentrations in polluted cases result in higher concentrations of ice, snow, and graupel/hail (Fig. 4d), similar to the dry/wet-season contrasts in simulated tropical continental deep convection in MD24. The enhanced condensation likely leads to detrainment after thermals reach neutral buoyancy, followed by the freezing of these cloud droplets via heterogeneous ice nucleation, gradually forming ice layers around the top of the convective clouds. Subsequent thermals entrain this ice and snow into droplet-rich thermal cores when penetrating the ice layers. This thermal-driven process promotes the generation of rimed particles (graupel/hail). Consequently, ice and snow particles exhibit a more homogeneous distribution along the thermal boundaries compared to other hydrometeors, which tend to be concentrated within the thermal cores. The subsequent figures provide a more thorough explanation of these processes.

The electrical properties (Fig. 4f,g) in the thermals show patterns consistent with the graupel-ice crystal collisional charging mechanism, as reviewed by Bruning et al. (2024). Charge density is larger in the same region where graupel and hail (Fig. 4e) are precipitating from the thermals. In the polluted cases, regions of greater ice and snow concentration above (but not at the center of) the thermal also show enhanced charge density. Electric potential shows the integrated effect of charge, with maxima in the clean case above and between the thermal's internal circulation, and extending to ice crystals laterally outside and above the thermal. The presence of thermal-internal potential gradients (i.e., electric fields) also suggests that flashes are more likely to initiate in the vicinity of thermals, as also inferred by Salinas et al. (2022); however, it was difficult to capture from this simulation due to the limited number of flash samples.

Figure 5 presents normalized histograms of thermal properties for both clean and polluted cases. The median of the thermal radii is approximately 0.7 km in both scenarios; however, the polluted case exhibits a tail extending to larger radii, reaching up to 2.3 km (Fig. 5a). Vertical velocity (W, Fig. 5b) and vertical travel distance ( $\Delta Z$ , Fig. 5c) are also marginally greater in the polluted case, while thermal entrainment rates are lower (Fig. 5f). This is consistent with findings by Hernandez-Deckers and Sherwood (2018), since entrainment is mainly determined by thermal size. Thermal lifetimes appear comparable between the two cases (Fig. 5e). The most distinct and interesting difference is the thermal initiation height ( $Z_0$ ), with the polluted case showing a median value approximately 0.5 km higher (Fig. 5d), and is discussed further in the following figure and analyses. This increased starting point, together with slightly faster thermals with similar lifetimes results in higher final altitudes (Fig. 5h). Also, the slightly faster and larger thermals result in slightly higher average mass flux (Fig. 5g). It should be noted that these differences are mostly small and that the total number of thermals tracked is less than half in the polluted cases compared to the clean cases.

Figure 6 illustrates the vertical profiles of thermal states under both polluted and clean atmospheric conditions. Analysis of the thermal number density (N, number of thermals per vertical bin and number of cells) in Figure 6a reveals a notable upward shift and increase in the vertical distribution of thermals above 3-4 km altitude in polluted conditions compared to clean conditions. Furthermore, vertical profiles of thermal radius and vertical velocity (Figs. 6b,c) indicate that the slightly





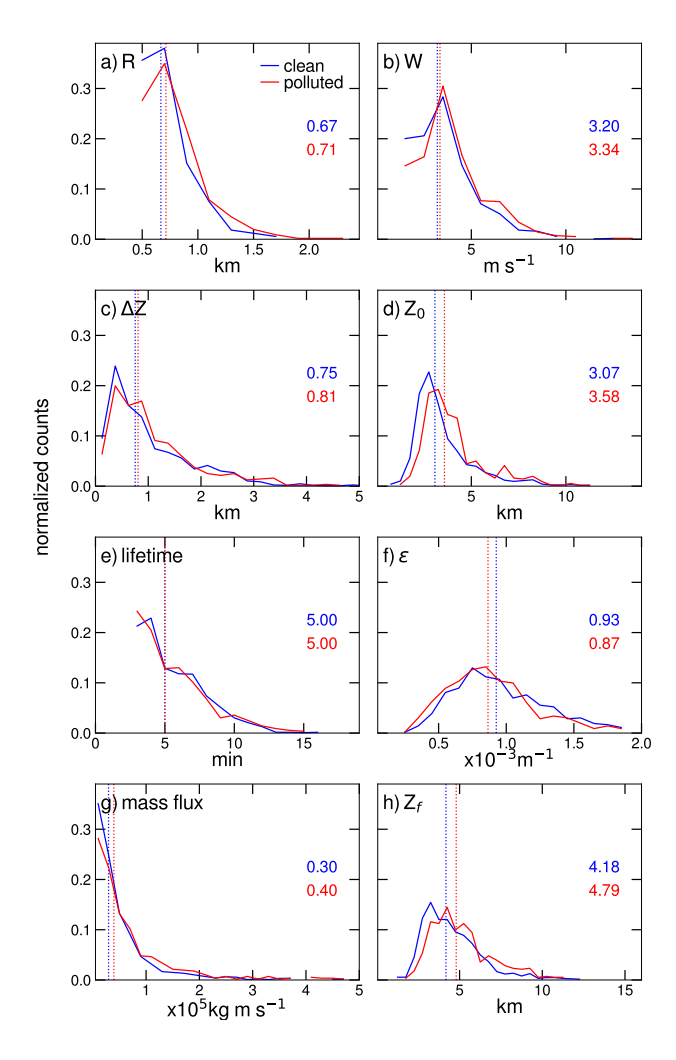


Figure 5. Histograms of (a) thermal radius R, (b) ascent rate W, (c) distance traveled  $\Delta Z$ , (d) starting height  $Z_0$ , (e) lifetime, (f) entrainment rate  $\varepsilon$ , (g) mass flux, and (h) final altitude  $Z_f$  for the clean cases (blue) and the polluted cases (red). Vertical dotted lines indicate the median values, which are annotated to the right of each figure.

larger thermals observed under polluted conditions are present at most altitudes. Concurrently, faster thermals are particularly prominent between 5-9 km in polluted environments.

Furthermore, the polluted scenario exhibits a substantial increase in cloud droplet (Qc) mixing ratio alongside a decrease in raindrop (Qr) mixing ratio (Figs. 6d,e). This microphysical shift leads to a greater abundance of ice and snow mixing ratios (Qi+s), attributed to the enhanced lofting of water above the melting layer. On the other hand, graupel and hail mixing ratios (Qg+h) increase slightly with polluted conditions between 6-8km, but decrease between 8-10km altitude. However, since there are more thermals between 6-8km than between 8-10km, the overall difference is an increase in graupel and hail (Fig. 4e).



305

320



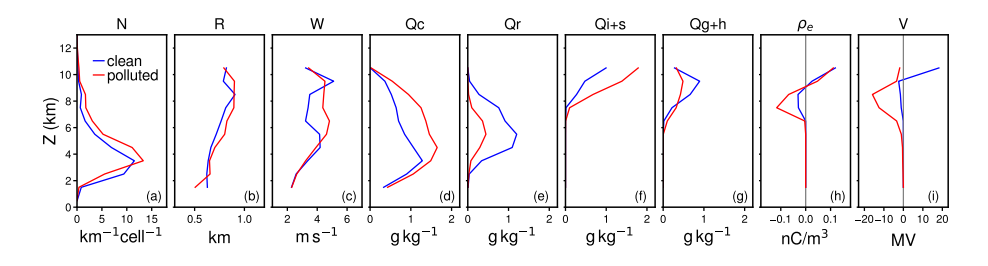


**Figure 6.** Vertical profiles of mean thermal properties: (a) thermal number density, (b) median thermal radius, (c) ascent rate, (d) cloud water mixing ratio, (e) rain water mixing ratio, (f) ice+snow mixing ratio, (g) graupel+hail mixing ratio, (h) volume charge density, and (i) electric potential. Median values in (b)-(i) are only shown where the number of thermals is at least 0.5% of the total sample size (6996 time steps for clean cases and 3126 for polluted cases).

While the population of thermals that reaches the charge-bearing layers is small, net-charge structure (Fig. 6h) produced by all thermals shows a positive-above-negative charge dipole in the upper mixed phase region, as observed. In observations, about 10% of flashes also discharge a lower-altitude negative-above-positive charge dipole just above the melting level, and as shown in Fig. 12, that lower charge dipole was present here and was therefore generated outside the thermal reference frame.

The lower (upper) charge in a dipole is typically carried on graupel (ice crystals), implying that only negative charging to graupel took place within the thermals. Enhancement of charge and potential in the polluted case (Figs. 4f,g and 6h,i) is primarily realized as a net enhancement of the negative charge center at 8 km altitude, consistent with less graupel aloft and more graupel at lower altitudes (Fig. 6g). The polluted case apparently has no effect on the net charge carried on ice crystals near 10 km, consistent with the generation of these species outside the thermal, as noted above. The net effect of enhancing the net charge and electrical potential on graupel enhances the electric potential overall, and therefore, from conservation of energy, should result in more flashes per thermal in the polluted cases, and as shown below, is what was modeled.

Fig. 7 presents cross-sectional composites of thermal properties at different altitude levels for the clean case. This averaging process, similar to that applied in Figure 4, weights the composite by the magnitude of the thermal mass flux at each reference level. Vertical velocity (W) tends to increase with elevation, reaching its peak at 8.5 km in this sample. Supersaturation (S) becomes discernible at 5.5 km and maximizes at 8.5 km, while significant cloud droplet (Qc) concentrations are primarily captured at lower elevations (2.5-4.5 km). Raindrop (Qr) concentrations peak at slightly higher elevations (2.5-6.5 km), which is associated with droplet loss due to the coalescence process.

These composites also reveal the evolution of variables within rising thermals. Notably, cloud water (Qc) is strongly coupled to the thermal's internal circulation, with its highest concentrations observed at the thermal's center where updraft velocities are strongest (DH22). Rainwater (Qr) development starts around 3 km altitude, coinciding with the region of most intense updrafts (W), and starts falling out from the thermal references. Conversely, the composites of ice and snow mixing ratios suggest that these particles are likely not generated within thermals in the mixed-phase zone, a finding consistent with MA24 regardless of the different sophistication of microphysics schemes (i.e., single- and double-moment microphysics with/without detailed nucleation schemes). Instead, ice crystals appear to form outside of thermals, likely originating from cloud water



330



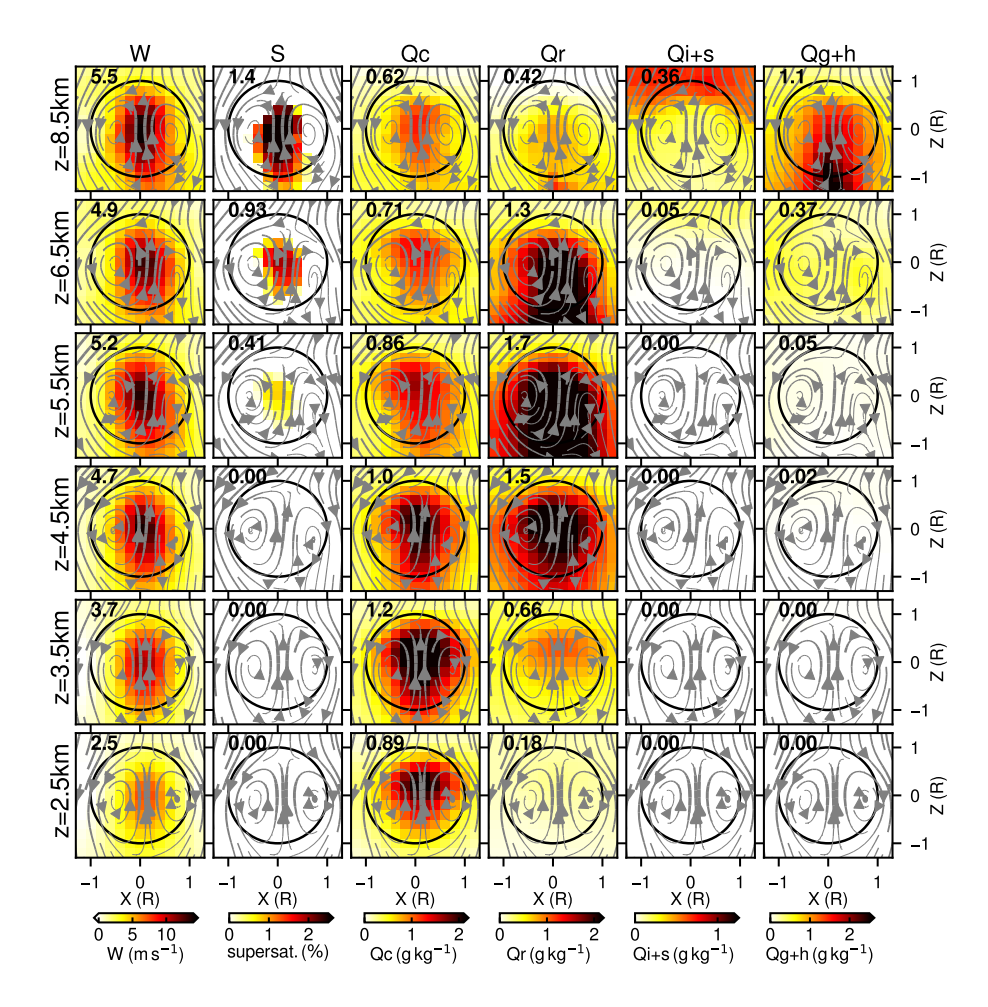


**Figure 7.** Cross sections of composites by altitude (rows) for (columns, left to right): vertical velocity, supersaturation with respect to water, cloud water mixing ratio, rain mixing ratio, ice+snow mixing ratio and graupel+hail mixing ratio, corresponding to the clean cases.

detrained from preceding thermals. Homogeneous distributions in the previous cross-section plot (Fig. 4d) also indicate this. As "younger" thermals subsequently penetrate this layer, where ice and snow are already present, the formation of graupel and hail is initiated.

Furthermore, ice and aggregation layers (Qi+s) are present and are entrained in thermals at the 6.5 and 8.5 km levels. Notably, graupel and hail particles (Qg+h) exhibit strong concentrations at the center of updraft core and also directly below the thermal cores at 8.5 km. This spatial distribution suggests that most of the riming process occurs at thermal cores due to the presence of thermal-generated droplets and entrained ice and snow aggregate particles in the mixed-phase level. This is in agreement with the thermal-driven graupel generation mechanism investigated in MA24 (including time-lapse analysis), despite differences in model dynamics, microphysics, and convective cases used in this study. The only differences from MA24 are the presence of cloud droplets well above the 0°C isothermal level (8.5 km), which is attributed to the treatment of super-cooled droplets



335

340

345

350

355

360

365



in a more sophisticated double-moment microphysics scheme used in this study, i.e., through single versus double moment microphysics with and without detailed cloud and ice nucleations.

It is also possible that riming between newly formed ice crystals at thermal core and existing droplets within the thermal contributes to in-thermal graupel generation. However, heterogeneous ice nucleation generation is generally weak at relatively warm temperatures (DeMott et al., 2010) compared with those characteristic of homogeneous nucleation levels. In this context, the MA24 sequential thermal-driven graupel generation theory appears to provide a more plausible explanation; A more detailed thermal-by-thermal analysis will be required in future studies to better understand this process, since the present analysis combines both younger and older thermals.

Fig. 8 illustrates the differences in cross-sectional composites of thermal properties between polluted and clean atmospheric conditions at various altitude levels. The observed variations in these composites closely align with those presented in Figure 6. Specifically, the vertical velocity in the polluted case appears stronger around 5.5-6.5 km altitude compared to the clean case. Regarding microphysical constituents, cloud droplet (Qc) concentrations are predominantly larger in the polluted case, whereas raindrop (Qr) concentrations are greater in the clean cases. Due to limited condensation, supersaturation (S) is observed to be larger in the clean cases. Polluted case enhanced ice and snow aggregate (Qi+s) concentrations at 8.5km due to enhanced cloud droplet (Qc) concentrations, but graupel and hail (Qg+h) concentration are mixed results at this level, as it is shown in Fig. 6g. Taken together with Fig. 6, these thermal composites clearly demonstrate the impact of background aerosol number concentrations on the simulated thermal dynamics and, consequently, on updraft core microphysical processes.

# 3.2 Changes in mesoscale environment

The aerosol sensitivities of cumulus thermal properties raise a critical question: What mechanisms drive these responses? Specifically, is this sensitivity primarily due to isolated microphysical feedback from warm- and/or cold-phase processes, or is it a consequence of time-sequential mesoscale environmental changes? Recent extensive reviews of aerosol-deep convection interactions have reached contrasting conclusions. Varble et al. (2023) summarized that warm-phase (condensation impact) is theoretically feasible, but observationally weak at most, while cold-phase (freezing impact) is theoretically unrealistic, emphasizing methodological flaws and limited robustness in prior studies. In contrast, Fan et al. (2025) contend that aerosol invigoration remains plausible under specific meteorological and aerosol conditions, particularly in relatively clean environments. Together, these perspectives underscore that the complexity of mesoscale environments and thermodynamic feedback presents substantial challenges to quantifying the impacts of aerosols on deep convection.

To address this question, first, the time series of all-sky full-domain-mean differences in hydrometeor and thermodynamic profiles are depicted (Fig. 9). The left and right columns of the profiles represent the 4 August and 7 August cases, respectively. Each profile illustrates the differences between the polluted and clean cases for various quantities. Red shading indicates larger values in the polluted case, while blue shading signifies larger values in the clean case.

Cloud droplet mixing ratios differences (dQc) are consistently positive (red shaded) throughout the sampling periods in both cases (Fig. 9a,g). This indicates that the polluted cases exhibit higher cloud droplet concentrations during these periods. Conversely, rain mixing ratio (dQr) differences are initially negative (blue shaded), suggesting a decrease in rain in the polluted



375



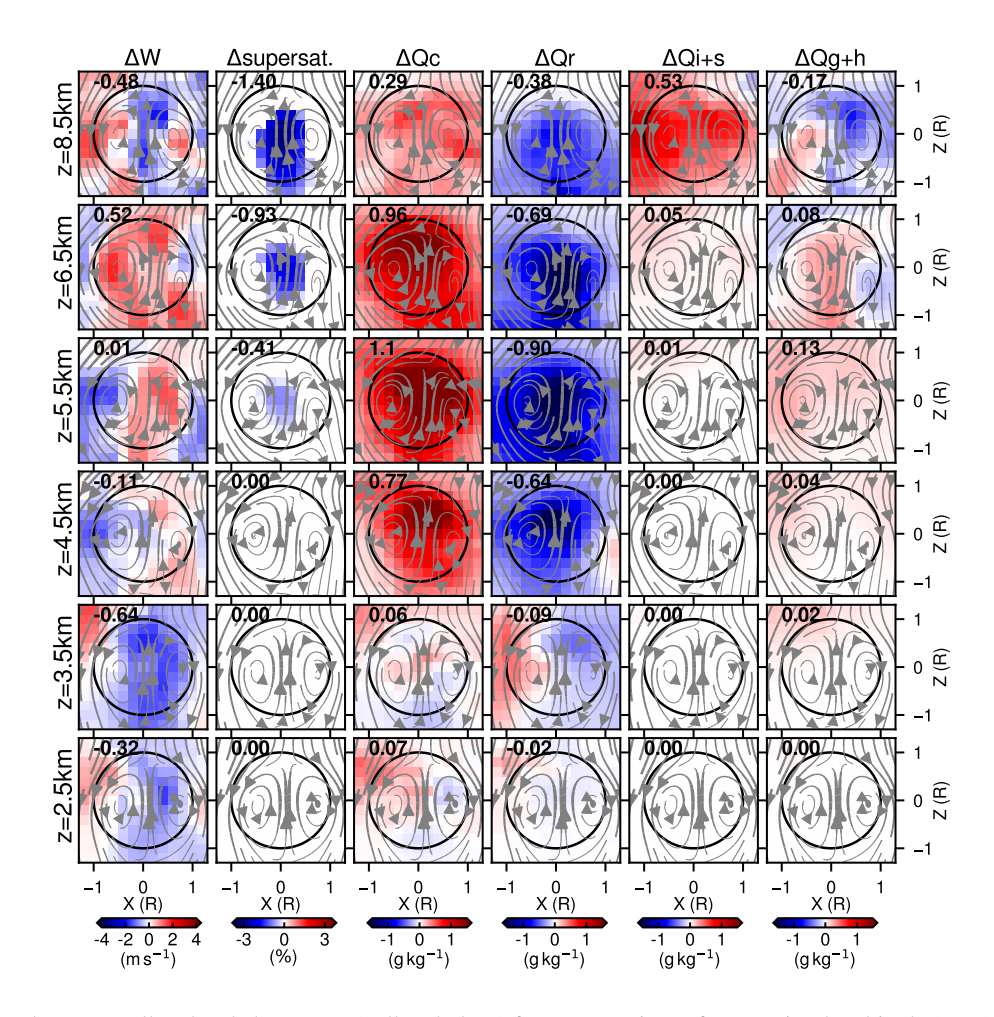


**Figure 8.** Difference between polluted and clean cases (polluted-clean) for cross sections of composites by altitude (rows) for (columns, left to right): vertical velocity, supersaturation, cloud water mixing ratio, rain mixing ratio, ice+snow mixing ratio and graupel+hail mixing ratio. The background wind fields are taken from the clean cases.

cases, but switch to positive differences (red shaded) in the last few hours, especially for the 7 August case (Fig. 9b,h). This period also exhibits clear increases in graupel and hail, suggesting enhanced cold-precipitation processes in the polluted case (Fig. 9d,j). Typically, a greater amount of Qc, associated with an increasing number of cloud droplets, tends to suppress warmrain production (Fig. 6 and as discussed in DH22).

The difference in water vapor (dQv) and air temperature (dT) appears to be relevant to those of cloud (dQc) and raindrops (dQr). Specifically, dQv remains consistently positive around 4-5 km height and near the surface (Fig. 9e,k), where dQc is also consistently positive, suggesting that the positive dQv is likely due to greater evaporation of cloud droplets in the polluted cases. Xue and Feingold (2006) conducted LES simulations of trade cumuli, demonstrating a coherent vertical structure between droplet evaporation fate and cloud liquid water content. Conversely, dQv is strongly negative around 2-3 km height, which



385



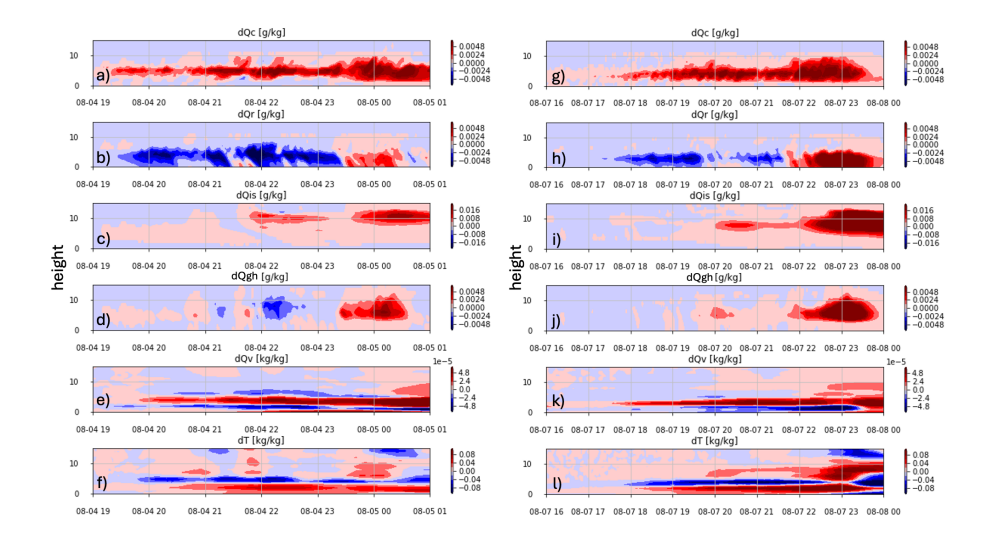


**Figure 9.** All-sky full-domain mean profile of polluted-clean differences in a&g) cloud droplet mass mixing ratio (dQc), b&h) rain mixing ratio (dQr), c&i) ice and snow mixing ratio (dQis), d&j) graupel and hail mixing ratio (dQgh), e&k) water vapor mixing ratio (dQv), f&l) air temperature (dT). The left (right) column shows 4 August (7 August) cases.

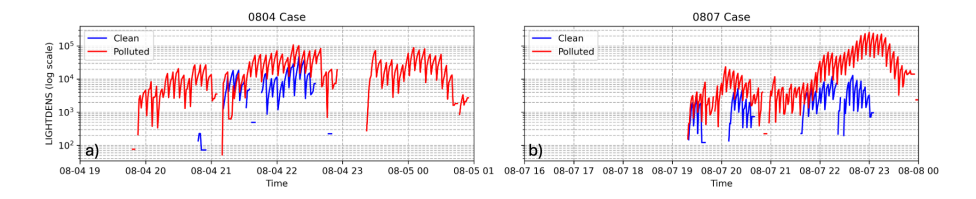


Figure 10. Time series of column lightning flash density (LIGHTDENS) from the clean and polluted cases.

we attribute to the greater evaporation of raindrops in the clean cases. Consequently, air temperature exhibits opposite signs of change at different heights compared to these hydrometeor profiles (Fig. 9f,l); i.e., more water vapor due to raindrop evaporation cools the air temperature. Typically, full-domain averaging incorporates a mixture of air masses and therefore exhibits some inconsistencies (e.g., enhanced near-surface evaporation in the polluted case). Nevertheless, the overall temperature and water vapor responses remain consistent throughout the analysis period.

Other consistent signals due to enhanced aerosols is the simulated column lightning density, exhibiting substantial differences between polluted and clean atmospheric conditions (Fig. 10). Despite only a slight increase in graupel and hail, the polluted case showed enhanced lightning densities, whereas the clean case frequently produced no lightning at all (e.g., 19:00-21:00 UTC on 4 August). The greater production of lightning flashes in the polluted case was also associated with the dominance of cloud ice and snow, largely due to enhanced cloud droplet freezing (Fig. 9). Increased lightning activity in the polluted case was both immediate and consistent throughout intense convective periods, agreeing with the thermal tracking analyses that clearly indicate the immediate impact of aerosols on convective microphysics.





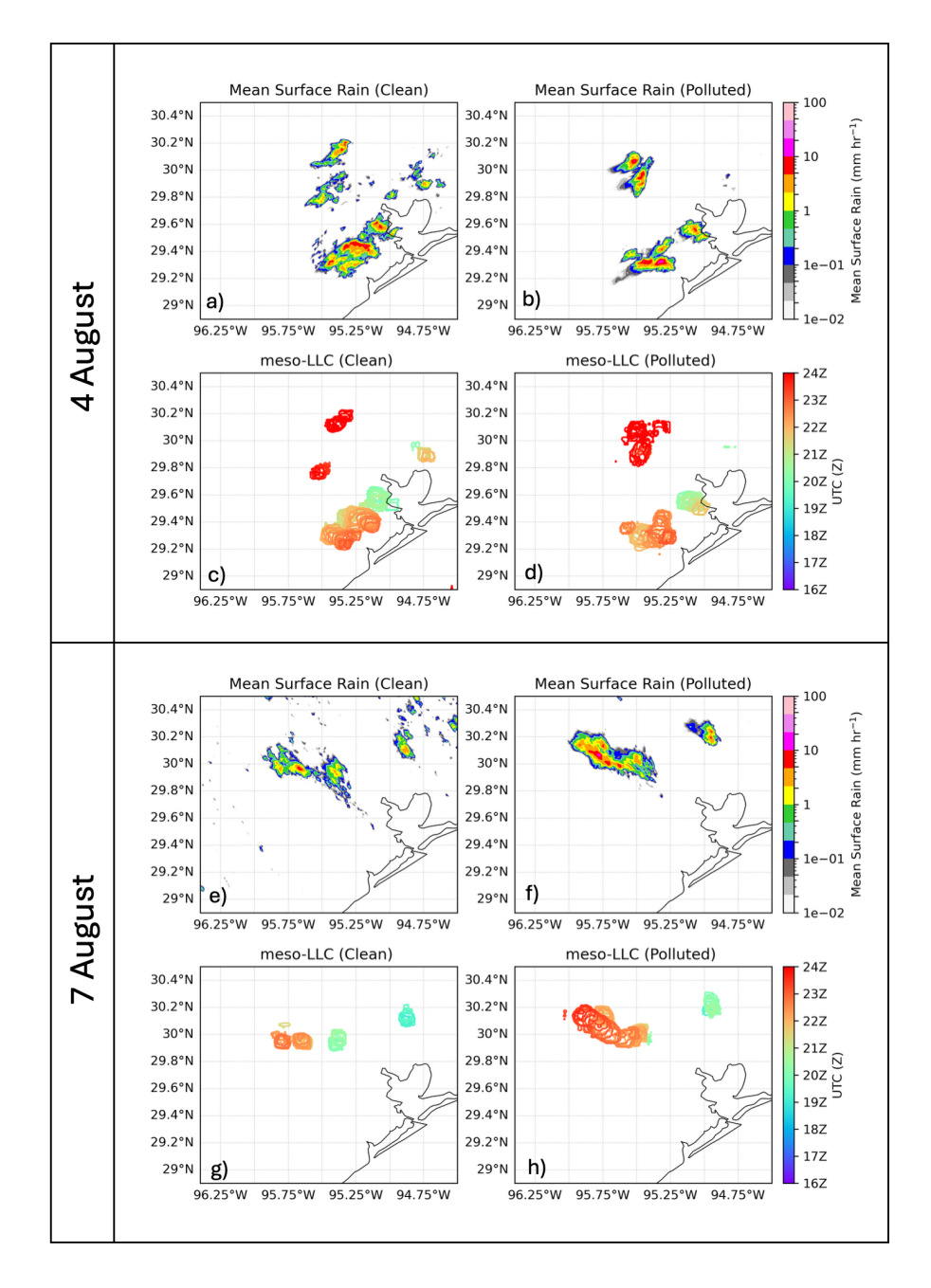


Figure 11. a-b,e-f) Mean surface precipitation and c-d,g-h) time evolutions of meso-LLC from 16Z to 24Z for 4 August and 7 August cases. The left and right column shows clean and polluted cases, respectively. The boundaries of meso-LLC are defined using a threshold of  $8 \times 10^{-5} \text{s}^{-1}$ , and are shaded according to their corresponding UTC time.



390

395

400

405

410

415

420



To understand the time-space evolution of mesoscale environment and precipitation, mesoscale low-level wind convergence (meso-LLC) fields are derived and analyzed. First, the simulated wind convergence was computed for each grid cell and then averaged between surface and 5 km altitude to generate LLC fields. Second, they are spatially averaged over 10 km x 10 km horizontal window to define meso-LLC. The meso-LLC field is a critical parameter that determines the exact location and timing of deep convection and microphysics development (e.g., Birch et al., 2013).

The temporal evolution of meso-LLC boundaries corresponds closely to the peak locations of the time-averaged surface rainfall fields (Fig. 11). Several clusters of meso-LLC developed during the analysis period, generally appearing at different locations, because of the sea-breeze-driven isolated convective cases. In the final hours, however, meso-LLCs (red contours) became more tightly clustered in the polluted cases compared to the clean cases on both 4 August and 7 August. In particular, the polluted case on 7 August exhibited markedly stronger and more consolidated clusters than the corresponding clean case. Consequently, rainfall in the polluted runs tended to be organized into fewer, larger groups, whereas rainfall in the clean runs was more dispersed into multiple smaller groups. Similar behavior has been reported in previous aerosol-deep convection simulation studies, although the storm types differ (e.g., Iguchi et al., 2020).

It is important to note that these changes in meso-LLC fields are purely driven by aerosol influences on cloud microphysics, as aerosol direct (e.g., radiation) effects were not considered in these sensitivity experiments. Both experiments also utilized identical initial and lateral boundary conditions, but different initial aerosol number concentrations in the polluted and clean cases (Section 2.2). In earlier times (until 20Z), the polluted case does not enhance cold-phase precipitation (Fig. 9b-h), while the polluted case consistently increases condensation and droplet number, suppresses warm-rain formation, and increases cloud ice and lightning discharge (Fig. 10). Appreciable strengthening only occurred in the late convective stage—suggesting a time-sequential impact on the mesoscale environment.

To verify this hypothesis, additional numerical sensitivity experiments were conducted to isolate the in-storm microphysics impact of aerosols on convective clouds from the impact of mesoscale environmental change, particularly for the 7 August case. Although the original simulations were initiated with "clean" and "polluted" conditions (Section 2.2), prolonged integration allows for the evolution of unique cloud, mesoscale environments, and CCN loss after nearly a day of simulation time. Thus, CCN concentrations can be largely different from the initialized values. To reduce these uncertainties, aerosols were re-initialized at 22:00 UTC on August 7th for both the clean and polluted cases. These are the times when the polluted runs enhance cold-precipitation processes (Fig. 9) associated with consolidated meso-LLC fields (Fig. 11).

Table 2 lists the names of the experiments. Note that the CleanRun(ReClean) and PollRun(RePolluted) experiments are specifically designed to make sure re-initializing clean/polluted aerosol conditions as described in Table 1, regardless of the altered aerosol concentrations from the initial conditions after 22 hours of integration.

Figure 12 (left column) shows vertical profiles of droplet number concentrations, rain, ice, and graupel mixing ratios, and total space charge averaged over the entire domain for all-sky conditions and from 22Z to 00Z (every 1 minute). The thick solid blue and red lines represent the original sensitivity experiments under clean (CleanRun(CTRL)) and polluted (PollRun(CTRL)) aerosol conditions, respectively, that evolved unique meso-LLC fields (Fig. 11). PollRun(CTRL) shows larger amounts of rain, ice, and graupel than CleanRun(CTRL) experiment during this time period, consistent with those of Fig 9. The magnitude of



430

435

440



**Table 2.** Experiment names and descriptions of the additional sensitivity simulations. Clean and polluted aerosol concentrations are defined in Table 1.

Experiment	Description		
CleanRun(CTRL)	Control (original) clean aerosol run		
CleanRun(ReClean)	Clean-aerosol run re-initialized with clean aerosols		
CleanRun(RePoll)	Clean-aerosol run re-initialized with polluted aerosols		
PollRun(CTRL)	Control (original) polluted-aerosols run		
PollRun(ReClean)	Polluted-aerosol run re-initialized with clean aerosols		
PollRun(RePolluted)	Polluted-aerosol run re-initialized with polluted aerosols		

total space change of PollRun(CTRL) shows more intensified multi-mode electric charging than CleanRun(CTRL), consistent with those of Fig. 10.

The PollRun(RePoll) and CleanRun(ReClean) experiments show slight differences from the CleanRun(CTRL) and Poll-Run(CTRL) experiments, respectively, suggesting that the spatial distributions of aerosol concentrations are altered through advection and aerosol microphysics loss throughout the model integration (Fig. 12, left column). All members of the polluted experiments (PollRun(CTRL), PollRun(ReClean), PollRun(RePoll)) show higher values of rain, ice, and graupel mixing ratios, and larger dipoles in total space charge than those of the clean experiments (CleanRun(CTRL), CleanRun(ReClean), CleanRun(RePoll)), suggesting that the mesoscale environment created by the PollRun(CTRL) experiment plays a dominant role in shaping the hydrometeor and electrification profiles.

Although not shown here, similar aerosol-reinitialization experiments were conducted for 4 August case, reinitializing polluted aerosols enhanced the cold-precipitation process. These results suggest that even over relatively short integration periods, the influence of aerosols on isolated deep convective cloud development strongly depends on the prevailing mesoscale environment, even within the single modeling framework employed in this study.

The right column of Fig. 12 shows similar profiles from the convective-core sampling, based on the minimum thresholds of column condensate (0.1g m<sup>-3</sup>) and maximum vertical velocity (greater than 4.0 m s<sup>-1</sup>). While domain all-sky sampling can quantify the total magnitude of hydrometeor profiles, the convective-core sampling shows that cloud droplet number concentrations (Nc) follow nearly identical values among the polluted-aerosol experiments group (PollRun(CTRL), PollRun(RePoll), and CleanRun(RePoll)), as well as among the clean-aerosol experiments group (CleanRun(CTRL), CleanRun(ReClean), and PollRun(ReClean)), regardless of the different mesoscale environment (Fig. 12b).

The large Nc also certainly reduces rain mixing ratio (Qr, Fig. 12d), and enhances ice mixing ratio (Qi, Fig. 12f) within the convective cores. As discussed earlier, charging outside thermals produces a weak positive charge center (Fig. 12j, between 5-6 km). The polluted experiment group (PollRun(CTRL), PollRun(RePoll), and CleanRun(RePoll)) also exhibit an upper-





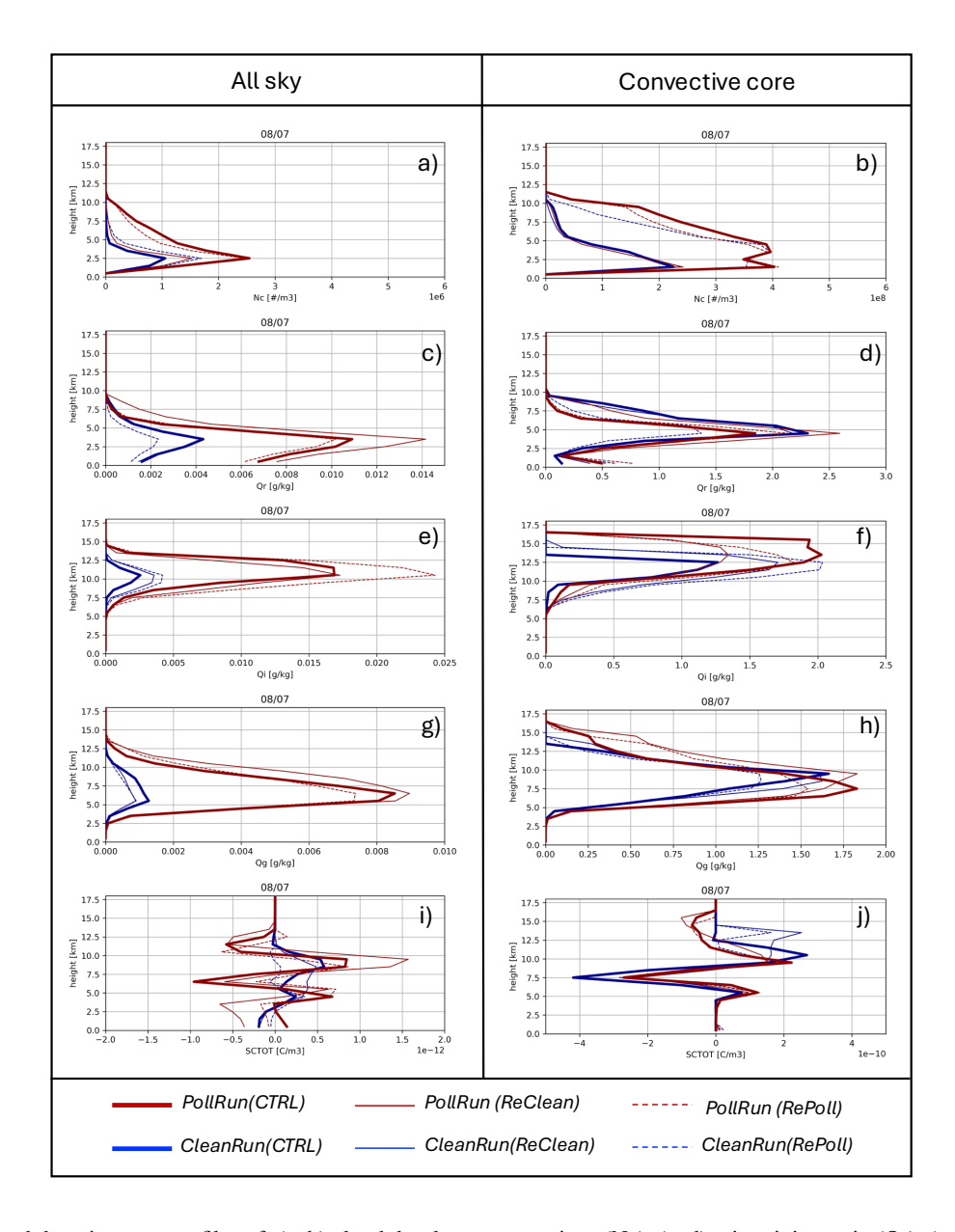


**Figure 12.** Time and domain mean profiles of: (a, b) cloud droplet concentrations (Nc), (c, d) rain mixing ratio (Qr), (e, f) ice mixing ratio (Qi), (g, h) graupel mixing ratio (Qg), and (i, j) total space charge (SCTOT) from the 7 August case. Note that the temporal integration is from 22:00Z to 24:00Z on 7 August. The left column shows all-sky (domain-wide) statistics; the right column shows convective-core statistics.

level negative charge center between 12-16 km, probably either due to relatively deep positive charging of graupel resulting in negative ice crystals aloft or due to screening layer formation from ion drift on longer-lived storm tops. Such enhancements to positive charging to graupel are expected, given the larger cloud droplet number concentrations modeled herein.



465

470

475

480



## 4 Summary and Discussion

This study conducted NU-WRF EPIC LESs for two golden cases (4 August, 2022 and 7 August, 2022) over the Houston area during the TRACER field campaign to investigate how aerosols impact sea-breeze-driven isolated deep convection. Each case was simulated with both low initial aerosol concentrations ("clean") and with high initial aerosol concentrations ("polluted") defined from the climatology of the field measurements. TOBAC was used to first identify isolated convective cells, within which then individual thermals were identified and tracked.

The polluted conditions exhibited more consolidated and less scattered convection, as well as lower numbers of isolated convective cells and thermals, albeit more thermals per cell. Based on composites of the tracked thermals by cases ("polluted" or "clean") and by elevation, several features were identified: regarding warm rain microphysical processes, it is found that higher aerosol concentrations increase droplet number concentrations, leading to the suppression of warm rain, and more water droplets being transported aloft, consistent with previous studies (e.g., Givati and Rosenfeld, 2004, HD22). In the same way as HD22, it is found that thermals act as water droplet generators and thus play a crucial role in this mechanism. As more cloud droplets reach higher levels, more ice and snow is produced.

With more sophisticated microphysics parameterization, our results, consistent with MA24, indicated that the ice and snow crystals are most likely formed outside of thermals in the mixed-phase zone, but ice formation require water droplets that have been detrained by dissipated thermals. Thus, thermals play an indirect role in ice formation, also suggesting the cold-phase invigoration (Rosenfeld et al., 2008) is not supported from our thermal analysis. However, thermals become once more directly responsible for the formation of graupel and hail, as subsequent thermals inject supercooled water droplets to these layers where ice and snow are already present. Thus, more supercooled droplets in the polluted case add more riming and graupel production in the thermals. Therefore, more graupel and hail could be produced in the polluted cases at lower levels of the mixed-phase zone, as more ice and snow crystals are available, which depicts more detailed paths of aerosol-cloud interactions within the convective cores than previous studies (Rosenfeld et al., 2008).

The electrification properties of clouds were also investigated using the model's parameterization of cloud electrification and bulk discharge processes. Consistent with enhanced graupel and hail, which imply increased ice—crystal collisional charging, greater charge density, steeper electric potential gradients near thermals, and ultimately more flashes were produced in the polluted simulations, consistent with the findings of Hu et al. (2019).

However, apart from the responses of microphysical properties, responses in terms of other properties of thermals are rather subtle, except that they tend to initiate at higher elevations in the polluted simulations, therefore suggesting a general upward shift in the location of thermals, and thus convection. Thermal entrainment rates are also slightly smaller in the polluted simulation than in the clean ones, consistent with slightly larger thermals. Otherwise, a weak increase in size and vertical velocity is also found for the polluted cases. This slightly higher vertical velocity could imply a limited invigorating effect due to aerosol warm-phase, but does not support cold-phase invigoration theories due to the limited ice formation within thermals. These results agree with detailed process modeling (Grabowski and Morrison, 2020) as well as with idealized 1D parcel model (Igel and van den Heever, 2021).



490

495

500

505



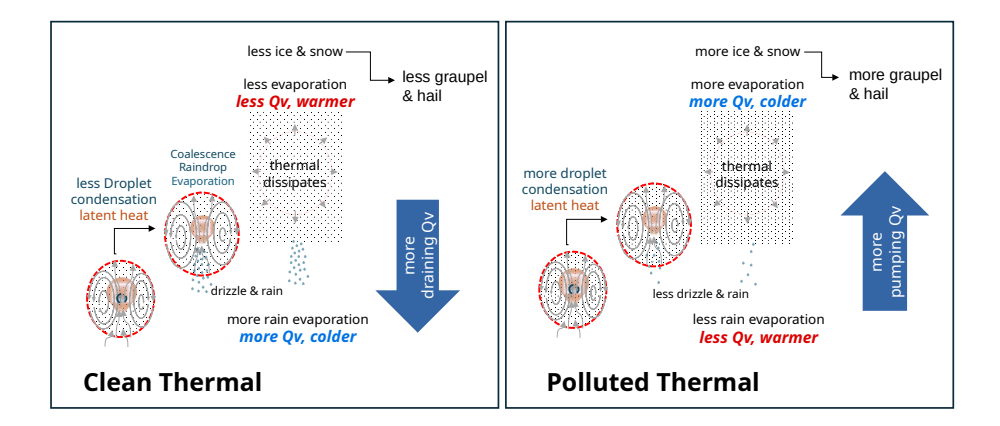


Figure 13. Thermal-driven cloud-scale aerosol feedback mechanisms.

Our domain-wide analyses and additional sensitivity experiments indicate that the background aerosol concentrations gradually perturb vertical profiles of water vapor and temperature through the thermals' contributions. Fig. 13 illustrates how the aerosol concentrations can affect water vapor profiles through thermal morphologies identified through the analyses. The polluted case tends to have slightly stronger convergence and updraft in the warm-phase clouds (not shown here) so that it could evaporate cloud droplets at elevated levels once they are lifted by thermals, resulting in pumping more boundary-layer water vapor to higher levels. Conversely, clean-case cumulus thermals generate more warm rain through the coalescence of cloud droplets, with sedimented raindrops evaporating at lower levels. This process brings down water vapor to lower elevation levels, thus "draining" water vapor. At this stage of warm-phase clouds, the polluted aerosol concentrations do not induce warm-phase invigoration, but provide consistent changes in water vapor vertical profiles.

Note that our investigation does not include direct measurements of evaporation and condensation rate; however, LES studies from Xue and Feingold (2006) demonstrated that higher aerosol concentrations enhance overall cloud evaporation, and net evaporation (condensation minus evaporation) becomes larger near the cloud top, where net condensation becomes peaked near cloud base, therefore supporting our idea. This unique evaporation process also induces a temperature feedback, with more evaporation of cloud droplets aloft in the polluted cases, which induces a cooling, whereas less evaporation of raindrops at lower levels implies a warming relative to the clean cases.

The changes in temperature and water vapor profiles, together with cloud radiative forcing, likely change the mesoscale environment to enhance cold-precipitation processes toward the end of the simulation period in the polluted cases. In particular, the mesoscale convergence field in the 7 August polluted simulation became sufficiently consolidated and robust to initiate a sequence of deep convective events between 22Z and 24Z. Additional sensitivity experiments showed that re-initialized aerosol concentrations slightly modified the vertical distributions of hydrometeors and electrification within convective cores; however, the overall intensity and spatial extent of convection were governed primarily by the mesoscale environment.

This result seems to be consistent with the mechanism proposed by Abbott and Cronin (2021), whereby higher aerosol concentrations lead to clouds lofting more condensate. The additional condensate moistens the surrounding environment,



515

520



reducing buoyancy dilution and ultimately enhancing larger-scale ascent and convection. In our case, however, the relevant timescale is only one day, substantially shorter than the 60-day integration reported by Abbott and Cronin (2021). Fan et al. (2025) summarize the recent studies related to aerosol impact through feedback between circulation and meteorology. They argue that a large-domain (>500 km) simulation setup is required to capture such feedback mechanism. However, our results capture the dramatic change in mesoscale environment using relatively small regional LES domain within 24-hour integration.

This complexity of aerosol-deep convective interaction likely contributes to the diversity reported by aerosol-cloud interaction model intercomparison projects (MIPs) in sea-breeze environment (Marinescu et al., 2021; Saleeby et al., 2025; van den Heever et al., 2025). While increased background aerosol concentrations can similarly enhance cloud droplet numbers and suppress warm-rain processes across different cloud-resolving models, evolution of mesoscale environments strongly varies across different models. This variability is likely attributed to differences in dynamic cores and microphysics packages, which induce unique mesoscale cloud feedback and rest of cloudiness and precipitation fields. At least, quantifications of changes in mesoscale environment will be required for future MIP activities.

Most recently, Wang et al. (2025) provide one of the first observational, conditional analyses of aerosol impacts on isolated deep convection using ground-based measurements from the TRACER campaign. This analysis enhances the understanding of how aerosol loading influences convective properties while acknowledging context dependence and uncertainties. It is possible to generate observation-equivalent fields from the NU-WRF EPIC framework and conduct similar sampling and systematic analysis from the simulated instrument-observables parameters to verify this process in the future.

Other noteworthy future effort includes more gradual perturbations of aerosol concentrations (e.g., DH22), rather than the extreme clean and polluted conditions examined in this study. Perturbing different aerosol size modes (coarse, accumulation, and Aitken) would also help clarify the role of fine-mode aerosols (Yin et al., 2024). To better capture gradual perturbations in the mesoscale environment, additional sensitivity experiments will be needed, including (1) modifying the latent heat of raindrop evaporation to assess temperature and pressure impact on sea-breeze circulation, and (2) adjusting cloud radiative forcing to evaluate the influence of cloud–radiation feedbacks on land–sea-breeze circulations. These topics are beyond the scope of the present study but are expected for the next pathway.

Code and data availability. The NASA Data Portal hosts (1) codes and plots for mesoscale environment analyses (https://portal.nccs.nasa.gov/datashare/cloudlibrary/TRACER/TRACER\_ACP2025.tar.gz) and (2) thermal tracking and analysis codes (https://portal.nccs.nasa.gov/datashare/cloudlibrary/THERMAL/). The data from the Scanning Mobility Particle Sizer (SMPS) at the Atmospheric Radiation Measurement (ARM) user facility site are available at http://dx.doi.org/10.5439/1476898.

Author contributions. TM and DHD prepared the manuscript with contributions from all authors. TI designed and performed the NU-WRF simulations. TS and CK prepared the aerosol concentrations and the related section. KB and EB developed and ran the TOBAC cell tracking algorithm. DH developed the thermal tracking algorithm, adapted it for tracking within the TOBAC tracked cells and prepared the thermal analysis figures. TM performed the mesoscale response analysis and prepared the related figures. MJ conducted TRACER field campaign.





Competing interests. The authors declare that at present they have no conflict of interest.

Acknowledgements. This work is funded by the US the Department of Energy (DOE) Atmospheric System Research (ASR) program (Pro540 gram Managers: Drs. Shaima Nasiri and Jeff Stehr, Grant DE-SC0021247 [UMD], DE-SC0012704 [BNL]), NASA CLOUDSAT AND
CALIPSO SCIENCE TEAM (CCST) program (Program Manager: Dr. David B. Considine, Grant 80NSSC23K0124), Toshi Matsui and
Scott Braun are also funded by the NASA Atomosphere Observing System mission (Program Scientist: Dr. William McCarty). We also
thank the NASA Center for Climate Simulation (NCCS) (Program Manager: Dr. Tsengdar Lee) for providing the computational resources to
conduct and analyze the NU-WRF EPIC simulations.





#### 545 References

560

- Abbott, T. H. and Cronin, T. W.: Aerosol invigoration of atmospheric convection through increases in humidity, Science, 371, 83–85, https://doi.org/10.1126/science.abc5181, 2021.
- Abdul-Razzak, H. and Ghan, S. J.: A parameterization of aerosol activation: 2. Multiple aerosol types, J. Geophys. Res., 105, 6837–6844, https://doi.org/10.1029/1999JD901161, 2000.
- Ackerman, A. S., Toon, O. B., Stevens, D. E., Heymsfield, A. J., Ramanathan, V., and Welton, E. J.: Reduction of Tropical Cloudiness by Soot, Science, 288, 1042–1047, https://doi.org/10.1126/science.288.5468.1042, 2000.
  - Albrecht, B. A.: Aerosols, Cloud Microphysics, and Fractional Cloudiness, Science, 245, 1227–1230, https://doi.org/10.1126/science.245.4923.1227, 1989.
- Andreae, M. O., Rosenfeld, D., Artaxo, P., Costa, A. A., Frank, G. P., Longo, K. M., and Silva-Dias, M. A. F.: Smoking Rain Clouds over the Amazon, Science, 303, 1337–1342, https://doi.org/10.1126/science.1092779, 2004.
  - Arakawa, A. and Schubert, W. H.: Interaction of a Cumulus Cloud Ensemble with the Large-Scale Environment, Part I, J. Atmos. Sci., 31, 674–701, https://doi.org/10.1175/1520-0469(1974)031<0674:IOACCE>2.0.CO;2, 1974.
  - Birch, C. E., Parker, D. J., O'Leary, A., Marsham, J. H., Taylor, C. M., Harris, P. P., and Lister, G. M. S.: Impact of soil moisture and convectively generated waves on the initiation of a West African mesoscale convective system, Quart. J. Roy. Meteorol. Soc., 139, 1712–1730, https://doi.org/10.1002/qj.2062, 2013.
  - Blyth, A. M., Lasher-Trapp, S. G., and Cooper, W. A.: A study of thermals in cumulus clouds, Quart. J. Roy. Meteorol. Soc., 131, 1171–1190, https://doi.org/10.1256/qj.03.180, 2005.
  - Bruning, E. C., Brunner, K. N., van Lier-Walqui, M., Logan, T., and Matsui, T.: Lightning and Radar Measures of Mixed-Phase Updraft Variability in Tracked Storms during the TRACER Field Campaign in Houston, Texas, Mon. Weather Rev., 152, 2753–2769, https://doi.org/10.1175/MWR-D-24-0060.1, 2024.
  - Chen, F., Kusaka, H., Bornstein, R., Ching, J., Grimmond, C. S. B., Grossman-Clarke, S., Loridan, T., Manning, K. W., Martilli, A., Miao, S., Sailor, D., Salamanca, F. P., Taha, H., Tewari, M., Wang, X., Wyszogrodzki, A. A., and Zhang, C.: The integrated WR-F/urban modelling system: development, evaluation, and applications to urban environmental problems, Int. J. Climatol., 31, 273–288, https://doi.org/10.1002/joc.2158, 2011.
- Chou, M.-D. and Suarez, M. J.: A Solar Radiation Parameterization for Atmospheric Studies, Tech. Rep. NASA/TM-1999-104606, Vol. 15, NASA Goddard Space Flight Center, Greenbelt, Maryland, 1999.
  - Chou, M.-D., Suarez, M. J., Liang, X.-Z., and Yah, M. M.-H.: A Thermal Infrared Radiation Parameterization for Atmospheric Studies, Tech. Rep. NASA/TM-2001-104606, Vol. 19, NASA Goddard Space Flight Center, Greenbelt, Maryland, 2001.
- Damiani, R., Vali, G., and Haimov, S.: The Structure of Thermals in Cumulus from Airborne Dual-Doppler Radar Observations, J. Atmos. Sci., 63, 1432–1450, https://doi.org/10.1175/JAS3701.1, 2006.
  - DeMott, P. J., Prenni, A. J., Liu, X., Kreidenweis, S. M., Petters, M. D., Twohy, C. H., Richardson, M. S., Eidhammer, T., and Rogers, D. C.: Predicting global atmospheric ice nuclei distributions and their impacts on climate, Proc. Nat. Acad. Sci. USA, 107, 11 217–11 222, https://doi.org/10.1073/pnas.0910818107, 2010.
  - Emanuel, K.: Atmospheric Convection, Oxford University Press, New York, 1994.





- Fan, J., Zhang, Y., Li, Z., Yan, H., Prabhakaran, T., Rosenfeld, D., and Khain, A.: Unveiling Aerosol Impacts on Deep Convective Clouds: Scientific Concept, Modeling, Observational Analysis, and Future Direction, J. Geophys. Res., 130, e2024JD041931, https://doi.org/10.1029/2024JD041931, 2025.
  - Fierro, A. O., Mansell, E. R., MacGorman, D. R., and Ziegler, C. L.: The Implementation of an Explicit Charging and Discharge Lightning Scheme within the WRF-ARW Model: Benchmark Simulations of a Continental Squall Line, a Tropical Cyclone, and a Winter Storm, Mon. Weather Rev., 141, 2390–2415, https://doi.org/10.1175/MWR-D-12-00278.1, 2013.
  - Fridlind, A. M., Li, X., Wu, D., van Lier-Walqui, M., Ackerman, A. S., Tao, W.-K., McFarquhar, G. M., Wu, W., Dong, X., Wang, J., Ryzhkov, A., Zhang, P., Poellot, M. R., Neumann, A., and Tomlinson, J. M.: Derivation of aerosol profiles for MC3E convection studies and use in simulations of the 20 May squall line case, Atmos. Chem. Phys., 17, 5947–5972, https://doi.org/10.5194/acp-17-5947-2017, 2017.
- Friedl, M., McIver, D., Hodges, J., Zhang, X., Muchoney, D., Strahler, A., Woodcock, C., Gopal, S., Schneider, A., Cooper, A., Baccini, A., Gao, F., and Schaaf, C.: Global land cover mapping from MODIS: algorithms and early results, Remote Sens. Environ., 83, 287–302, https://doi.org/10.1016/S0034-4257(02)00078-0, 2002.
  - Givati, A. and Rosenfeld, D.: Quantifying Precipitation Suppression Due to Air Pollution, J. Appl. Meteorol., 43, 1038–1056, https://doi.org/10.1175/1520-0450(2004)043<1038:QPSDTA>2.0.CO;2, 2004.
- 595 Grabowski, W. W. and Morrison, H.: Do Ultrafine Cloud Condensation Nuclei Invigorate Deep Convection?, J. Atmos. Sci., 77, 2567–2583, https://doi.org/10.1175/JAS-D-20-0012.1, 2020.
  - Gu, J.-F., Stephen Plant, R., Holloway, C. E., and Muetzelfeldt, M. R.: Pressure Drag for Shallow Cumulus Clouds: From Thermals to the Cloud Ensemble, Geophys. Res. Lett., 47, e2020GL090460, https://doi.org/10.1029/2020GL090460, 2020.
- Harkema, S. S., Mansell, E. R., Fierro, A. O., Carey, L. D., Schultz, C. J., Matsui, T., and Berndt, E. B.: Explicitly Resolving Light-600 ning and Electrification Processes From the 10–12 April 2019 Thundersnow Outbreak, J. Geophys. Res., 129, e2023JD039987, https://doi.org/10.1029/2023JD039987, 2024.
  - Heikenfeld, M., Marinescu, P. J., Christensen, M., Watson-Parris, D., Senf, F., van den Heever, S. C., and Stier, P.: tobac 1.2: towards a flexible framework for tracking and analysis of clouds in diverse datasets, Geosci. Model Dev., 12, 4551–4570, https://doi.org/10.5194/gmd-12-4551-2019, 2019.
- Hernandez-Deckers, D. and Sherwood, S. C.: A numerical study of cumulus thermals, J. Atmos. Sci., 73, 4117–4136, https://doi.org/10.1175/JAS-D-15-0385.1, 2016.
  - Hernandez-Deckers, D. and Sherwood, S. C.: On the Role of Entrainment in the Fate of Cumulus Thermals, J. Atmos. Sci., 75, 3911–3924, https://doi.org/10.1175/JAS-D-18-0077.1, 2018.
- Hernandez-Deckers, D., Matsui, T., and Fridlind, A. M.: Updraft dynamics and microphysics: on the added value of the cumulus thermal reference frame in simulations of aerosol–deep convection interactions, Atmos. Chem. Phys., 22, 711–724, https://doi.org/10.5194/acp-22-711-2022, 2022.
  - Hersbach, H., Bell, B., Berrisford, P., Hirahara, S., Horányi, A., Muñoz-Sabater, J., Nicolas, J., Peubey, C., Radu, R., Schepers, D., Simmons, A., Soci, C., Abdalla, S., Abellan, X., Balsamo, G., Bechtold, P., Biavati, G., Bidlot, J., Bonavita, M., De Chiara, G., Dahlgren, P., Dee, D., Diamantakis, M., Dragani, R., Flemming, J., Forbes, R., Fuentes, M., Geer, A., Haimberger, L., Healy, S., Hogan, R. J., Hólm, E.,
- Janisková, M., Keeley, S., Laloyaux, P., Lopez, P., Lupu, C., Radnoti, G., de Rosnay, P., Rozum, I., Vamborg, F., Villaume, S., and Thépaut, J.-N.: The ERA5 global reanalysis, Quart. J. Roy. Meteorol. Soc., 146, 1999–2049, https://doi.org/10.1002/qj.3803, 2020.





- Hirt, M., Craig, G. C., Schäfer, S. A. K., Savre, J., and Heinze, R.: Cold-pool-driven convective initiation: using causal graph analysis to determine what convection-permitting models are missing, Quart. J. Roy. Meteorol. Soc., 146, 2205–2227, https://doi.org/10.1002/qj.3788, 2020.
- Hu, J., Rosenfeld, D., Ryzhkov, A., Zrnic, D., Williams, E., Zhang, P., Snyder, J. C., Zhang, R., and Weitz, R.: Polarimetric Radar Convective Cell Tracking Reveals Large Sensitivity of Cloud Precipitation and Electrification Properties to CCN, J. Geophys. Res., 124, 12194–12205, https://doi.org/10.1029/2019JD030857, 2019.
  - Igel, A. L. and van den Heever, S. C.: Invigoration or Enervation of Convective Clouds by Aerosols?, Geophys. Res. Lett., 48, e2021GL093 804, https://doi.org/10.1029/2021GL093804, 2021.
- Iguchi, T., Rutledge, S. A., Tao, W.-K., Matsui, T., Dolan, B., Lang, S. E., and Barnum, J.: Impacts of Aerosol and Environmental Conditions on Maritime and Continental Deep Convective Systems Using a Bin Microphysical Model, J. Geophys. Res., 125, e2019JD030952, https://doi.org/10.1029/2019JD030952, 2020.
  - Jensen, M. P., Flynn, J. H., Judd, L. M., Kollias, P., Kuang, C., Mcfarquhar, G., Nadkarni, R., Powers, H., and Sullivan, J.: A Succession of Cloud, Precipitation, Aerosol, and Air Quality Field Experiments in the Coastal Urban Environment, Bull. Amer. Meteorol. Soc., 103, 103–105, https://doi.org/10.1175/BAMS-D-21-0104.1, 2022.
  - Jensen, M. P., Flynn, J. H., Gonzalez-Cruz, J. E., Judd, L. M., Kollias, P., Kuang, C., McFarquhar, G. M., Powers, H., Ramamurthy, P., Sullivan, J., Aiken, A. C., Alvarez, S. L., Argay, P., Argrow, B., Bell, T. M., Boyer, D., Brooks, S. D., Bruning, E. C., Brunner, K., Butterworth, B., Calmer, R., Cappa, C. D., Chakrabarty, R. K., Chandrasekar, V., Chao, C.-Y., Chen, B., China, S., Collins, D. R., Collis, S. M., Crowell, S., Porto, R. D., de Boer, G., Deng, M., Dexheimer, D., Drager, A. J., Du, X., Dubey, M. K., Dzambo, A. M., Etten-Bohm,
- M., Fan, J., Farley, R., Feng, Y.-C., Feng, Y., Fenn, M., Ferrare, R. E., Flusche, S., Fridlind, A. M., Galewsky, J., Gamarro, H., Gardner, S., Ghate, V. P., Giangrande, S. E., Griffin, R. J., Griggs, T., Gronoff, G. P., Grover, M., Gaugenti, M., Guo, F., Gupta, S., Hu, J., Huang, Y., Jackson, R. C., Hair, J. W., Johnson, K. L., Kasparoglu, S., Klein, P., Kotsakis, A. E., Kumar, J., Kumjian, M. R., Lamer, K., Lappin, F. M., Lei, Z., Li, J., Li, R., Li, Y., Logan, T., Lombardo, K., Luke, E. P., Mages, Z., Matthews, A. A., Matthews, B. H., Mayol-Bracero, O., Matsui, T., McKeown, K. E., Mehra, M., Mei, F., Meskidzhe, N., Nguyen, C., Nielsen, E. R., Nowotarski, C. J., Oaks, D., Oktem, R., Oue,
- M., Park, J. M., Partida, N., Patil, S., Pena, J. C., Petters, M. D., Phoenix, D. B., Puthserry, J. V., Rapp, A. D., Romps, D. M., Roots, M., Rosenfeld, D., Saleeby, S. M., Savala, P., Sedlacek, A. J., Sharma, M., Sheesley, R., Shingler, T. J., Shrestha, S., Singh, A., Smith, E. N., Smith, J. N., Smith, S., Snyder, J., Spicer, E., Spinei, E., Spychala, M., Steir, P., Storm, M. R., Subba, T., Treserras, B. P., Trojanowski, R., Theisen, A., Thompson, S. A., Twigg, L., Uin, J., Ulinski, A. R., van den Heever, S., van Lier-Walqui, M., Varble, A. C., Wagner, T. J., Wakeen, J., Wales, N. A., Walter, P. J., Wang, D., Wang, J., Wood, L., Wang, Y., Wolde, M., Yoon, S., Young, M. H., Zawadowicz, M. A.,
- Zhang, Q., Zhou, A., Zhu, Z., and Zhu, Z.: Studying Aerosol, Clouds, and Air Quality in the Coastal Urban Environment of Southeastern Texas, Bull. Amer. Meteorol. Soc., https://doi.org/10.1175/BAMS-D-23-0331.1, 2025.
  - Khain, A. P., BenMoshe, N., and Pokrovsky, A.: Factors Determining the Impact of Aerosols on Surface Precipitation from Clouds: An Attempt at Classification, J. Atmos. Sci., 65, 1721–1748, https://doi.org/10.1175/2007JAS2515.1, 2008.
- Koontz, A., Uin, J., Andrews, E., Enekwizu, O., Hayes, C., and Salwen, C.: Cloud Condensation Nuclei Particle Counter (AOSCCN2COLASPECTRA), 2021-10-01 to 2022-09-02, ARM Mobile Facility (HOU), Houston, TX; AMF1 (main site for TRACER) (M1), https://doi.org/10.5439/1323896, 2021.
  - Koren, I., Kaufman, Y. J., Rosenfeld, D., Remer, L. A., and Rudich, Y.: Aerosol invigoration and restructuring of Atlantic convective clouds, Geophys. Res. Lett., 32, https://doi.org/10.1029/2005GL023187, 2005.





- Kusaka, H. and Kimura, F.: Coupling a Single-Layer Urban Canopy Model with a Simple Atmospheric Model: Impact on Urban Heat Island Simulation for an Idealized Case, J. Meteorol. Soc. Japan, 82, 67–80, https://doi.org/10.2151/jmsj.82.67, 2004.
  - Kusaka, H., Kondo, H., Kikegawa, Y., and Kimura, F.: A Simple Single-Layer Urban Canopy Model For Atmospheric Models: Comparison With Multi-Layer And Slab Models, Bound.-Lay. Meteorol., 101, 329–358, https://doi.org/10.1023/A:1019207923078, 2001.
  - Li, Z., Niu, F., Fan, J., Liu, Y., Rosenfeld, D., and Ding, Y.: Long-term impacts of aerosols on the vertical development of clouds and precipitation, Nature Geosci, 4, 888–894, https://doi.org/10.1038/ngeo1313, 2011.
- Lin, J. C., Matsui, T., Pielke Sr., R. A., and Kummerow, C.: Effects of biomass-burning-derived aerosols on precipitation and clouds in the Amazon Basin: a satellite-based empirical study, J. Geophys. Res., 111, https://doi.org/10.1029/2005JD006884, 2006.
  - Mansell, E. R., MacGorman, D. R., Ziegler, C. L., and Straka, J. M.: Charge structure and lightning sensitivity in a simulated multicell thunderstorm, J. Geophys. Res., 110, https://doi.org/10.1029/2004JD005287, 2005.
- Mansell, E. R., Ziegler, C. L., and Bruning, E. C.: Simulated Electrification of a Small Thunderstorm with Two-Moment Bulk Microphysics,

  J. Atmos. Sci., 67, 171–194, https://doi.org/10.1175/2009JAS2965.1, 2010.
  - Marinescu, P. J., van den Heever, S. C., Heikenfeld, M., Barrett, A. I., Barthlott, C., Hoose, C., Fan, J., Fridlind, A. M., Matsui, T., Miltenberger, A. K., Stier, P., Vie, B., White, B. A., and Zhang, Y.: Impacts of Varying Concentrations of Cloud Condensation Nuclei on Deep Convective Cloud Updrafts—A Multimodel Assessment, J. Atmos. Sci., 78, 1147–1172, https://doi.org/10.1175/JAS-D-20-0200.1, 2021.
- Matsui, T., Dolan, B., Iguchi, T., Rutledge, S. A., Tao, W.-K., and Lang, S.: Polarimetric Radar Characteristics of Simulated and Observed Intense Convective Cores for a Midlatitude Continental and Tropical Maritime Environment, J. Hydrometeor., 21, 501–517, https://doi.org/10.1175/JHM-D-19-0185.1, 2020a.
  - Matsui, T., Zhang, S. Q., Lang, S. E., Tao, W.-K., Ichoku, C., and Peters-Lidard, C. D.: Impact of radiation frequency, precipitation radiative forcing, and radiation column aggregation on convection-permitting West African monsoon simulations, Clim. Dynam., 55, 193–213, https://doi.org/10.1007/s00382-018-4187-2, 2020b.
- Matsui, T., Wolff, D. B., Lang, S., Mohr, K., Zhang, M., Xie, S., Tang, S., Saleeby, S. M., Posselt, D. J., Braun, S. A., Chern, J.-D., Dolan, B., Pippitt, J. L., and Loftus, A. M.: Systematic Validation of Ensemble Cloud-Process Simulations Using Polarimetric Radar Observations and Simulator Over the NASA Wallops Flight Facility, J. Geophys. Res., 128, e2022JD038134, https://doi.org/10.1029/2022JD038134, 2023.
- Matsui, T., Hernandez-Deckers, D., Giangrande, S. E., Biscaro, T. S., Fridlind, A., and Braun, S.: A thermal-driven graupel generation process to explain dry-season convective vigor over the Amazon, Atmos. Chem. Phys., 24, 10793–10814, https://doi.org/10.5194/acp-24-10793-2024, 2024.
  - Monin, A. and Obukhov, A.: Basic laws of turbulent mixing in the ground surface layer, Tr Geophiz Inst Akad Nauk SSSR, 151, 163–187, 1954.
- Morrison, H. and Peters, J. M.: Theoretical Expressions for the Ascent Rate of Moist Deep Convective Thermals, J. Atmos. Sci., 75, 1699–1719, https://doi.org/10.1175/jas-d-17-0295.1, 2018.
  - Morrison, H., Peters, J. M., Varble, A. C., Hannah, W. M., and Giangrande, S. E.: Thermal Chains and Entrainment in Cumulus Updrafts. Part I: Theoretical Description, J. Atmos. Sci., 77, 3637–3660, https://doi.org/10.1175/JAS-D-19-0243.1, 2020a.
- Morrison, H., van Lier-Walqui, M., Fridlind, A. M., Grabowski, W. W., Harrington, J. Y., Hoose, C., Korolev, A., Kumjian, M. R.,
   Milbrandt, J. A., Pawlowska, H., Posselt, D. J., Prat, O. P., Reimel, K. J., Shima, S.-I., van Diedenhoven, B., and Xue, L.:
   Confronting the Challenge of Modeling Cloud and Precipitation Microphysics, J. Adv. Model. Earth Syst., 12, e2019MS001689, https://doi.org/10.1029/2019MS001689, 2020b.



700

705

710



- Morrison, H., Jeevanjee, N., Lecoanet, D., and Peters, J. M.: What Controls the Entrainment Rate of Dry Buoyant Thermals with Varying Initial Aspect Ratio?, J. Atmos. Sci., 80, 2711 2728, https://doi.org/10.1175/JAS-D-23-0063.1, 2023.
- Nakanishi, M. and Niino, H.: An Improved Mellor–Yamada Level-3 Model: Its Numerical Stability and Application to a Regional Prediction of Advection Fog, Bound.-Lay. Meteorol., 119, 397–407, https://doi.org/10.1007/s10546-005-9030-8, 2006.
  - Nakanishi, M. and Niino, H.: Development of an Improved Turbulence Closure Model for the Atmospheric Boundary Layer, J. Meteorol. Soc. Japan, 87, 895–912, https://doi.org/10.2151/jmsj.87.895, 2009.
  - Niu, G.-Y., Yang, Z.-L., Mitchell, K. E., Chen, F., Ek, M. B., Barlage, M., Kumar, A., Manning, K., Niyogi, D., Rosero, E., Tewari, M., and Xia, Y.: The community Noah land surface model with multiparameterization options (Noah-MP): 1. Model description and evaluation with local-scale measurements, J. Geophys. Res., 116, https://doi.org/10.1029/2010JD015139, 2011.
  - Peters, J. M., Morrison, H., Varble, A. C., Hannah, W. M., and Giangrande, S. E.: Thermal Chains and Entrainment in Cumulus Updrafts. Part II: Analysis of Idealized Simulations, J. Atmos. Sci., 77, 3661–3681, https://doi.org/10.1175/JAS-D-19-0244.1, 2020.
  - Peters-Lidard, C. D., Kemp, E. M., Matsui, T., Santanello, J. A., Kumar, S. V., Jacob, J. P., Clune, T., Tao, W.-K., Chin, M., Hou, A., Case, J. L., Kim, D., Kim, K.-M., Lau, W., Liu, Y., Shi, J., Starr, D., Tan, Q., Tao, Z., Zaitchik, B. F., Zavodsky, B., Zhang, S. Q., and Zupanski, M.: Integrated modeling of aerosol, cloud, precipitation and land processes at satellite-resolved scales, Environmental Modelling & Software, 67, 149–159, https://doi.org/10.1016/j.envsoft.2015.01.007, 2015.
  - Romps, D. M. and Charn, A. B.: Sticky Thermals: Evidence for a Dominant Balance between Buoyancy and Drag in Cloud Updrafts, J. Atmos. Sci., 72, 2890–2901, https://doi.org/10.1175/JAS-D-15-0042.1, 2015.
  - Romps, D. M., Öktem, R., Endo, S., and Vogelmann, A. M.: On the Life Cycle of a Shallow Cumulus Cloud: Is It a Bubble or Plume, Active or Forced?, J. Atmos. Sci., 78, 2823–2833, https://doi.org/10.1175/JAS-D-20-0361.1, 2021.
  - Rosenfeld, D., Lohmann, U., Raga, G. B., O'Dowd, C. D., Kulmala, M., Fuzzi, S., Reissell, A., and Andreae, M. O.: Flood or Drought: How Do Aerosols Affect Precipitation?, Science, 321, 1309–1313, https://doi.org/10.1126/science.1160606, 2008.
  - Saleeby, S. M., van den Heever, S. C., Marinescu, P. J., Oue, M., Barrett, A. I., Barthlott, C., Cherian, R., Fan, J., Fridlind, A. M., Heikenfeld, M., Hoose, C., Matsui, T., Miltenberger, A. K., Quaas, J., Shpund, J., Stier, P., Vie, B., White, B. A., and Zhang, Y.: Model Intercomparison of the Impacts of Varying Cloud Droplet–Nucleating Aerosols on the Life Cycle and Microphysics of Isolated Deep Convection, J. Atmos. Sci., 82, 2197–2217, https://doi.org/10.1175/JAS-D-24-0181.1, 2025.
  - Salinas, V., Bruning, E. C., and Mansell, E. R.: Examining the Kinematic Structures within which Lightning Flashes Are Initiated Using a Cloud-Resolving Model, J. Atmos. Sci., 79, 513–530, https://doi.org/10.1175/JAS-D-21-0132.1, 2022.
- Saunders, P. M.: AN OBSERVATIONAL STUDY OF CUMULUS, J. Atmos. Sci., 18, 451–467, https://doi.org/10.1175/1520-0469(1961)018<0451:AOSOC>2.0.CO;2, 1961.
  - Scorer, R. S. and Ludlam, F. H.: Bubble theory of penetrative convection, Quart. J. Roy. Meteorol. Soc., 79, 94–103, https://doi.org/10.1002/qj.49707933908, 1953.
  - Seinfeld, J. and Pandis, S.: Atmospheric Chemistry and Physics: From Air Pollution to Climate Change, John Wiley & Sons, New York, 2006.
- Sherwood, S. C., Hernández-Deckers, D., Colin, M., and Robinson, F.: Slippery Thermals and the Cumulus Entrainment Paradox\*, J. Atmos. Sci., 70, 2426–2442, https://doi.org/10.1175/JAS-D-12-0220.1, 2013.
  - Singh, A. and Kuang, C.: Scanning Mobility Particle Sizer (SMPS) Instrument Handbook, Tech. Rep. DOE/SC-ARM-TR-147, U.S. Department of Energy, Atmospheric Radiation Measurement user facility, Richland, Washington., 2024.





- Skamarock, W. C., Klemp, J. B., Dudhia, J., Gill, D. O., Barker, D. M., Duda, M. G., Huang, X.-Y., Wang, W., and Powers, J. G.: A Description of the Advanced Research WRF Version 3, NCAR Technical Note NCAR/TN-475+STR. June 2008. Mesoscale and Microscale Meteorology Division. National Center for Atmospheric Research. Boulder, 475, 1, https://doi.org/10.5065/D68S4MVH, 2008.
  - Sokolowsky, G. A., Freeman, S. W., Jones, W. K., Kukulies, J., Senf, F., Marinescu, P. J., Heikenfeld, M., Brunner, K. N., Bruning, E. C., Collis, S. M., Jackson, R. C., Leung, G. R., Pfeifer, N., Raut, B. A., Saleeby, S. M., Stier, P., and van den Heever, S. C.: *tobac* v1.5: introducing fast 3D tracking, splits and mergers, and other enhancements for identifying and analysing meteorological phenomena, Geosci. Model Dev., 17, 5309–5330, https://doi.org/10.5194/gmd-17-5309-2024, 2024.
  - Stanford, M. W., Fridlind, A. M., Ackerman, A. S., van Diedenhoven, B., Xiao, Q., Wang, J., Matsui, T., Hernandez-Deckers, D., and Lawson, P.: Warm-phase microphysical evolution in large-eddy simulations of tropical cumulus congestus: evaluating drop size distribution evolution using polarimetry retrievals, in situ measurements, and a thermal-based framework, Atmos. Chem. Phys., 25, 11 199–11 231, https://doi.org/10.5194/acp-25-11199-2025, 2025.
- Stephens, G. L., Shiro, K. A., Hakuba, M. Z., Takahashi, H., Pilewskie, J. A., Andrews, T., Stubenrauch, C. J., and Wu, L.: Tropical Deep Convection, Cloud Feedbacks and Climate Sensitivity, Surveys in Geophys., 45, 1903–1931, https://doi.org/10.1007/s10712-024-09831-1, 2024.
  - Tao, W.-K., Chen, J.-P., Li, Z., Wang, C., and Zhang, C.: Impact of aerosols on convective clouds and precipitation, Rev. Geophys., 50, https://doi.org/10.1029/2011RG000369, 2012.
- 745 Twomey, S.: Pollution and the planetary albedo, Atmos. Environ. (1967), 8, 1251–1256, https://doi.org/10.1016/0004-6981(74)90004-3, 1974.
  - Uin, J., Aiken, A. C., Dubey, M. K., Kuang, C., Pekour, M., Salwen, C., Sedlacek, A. J., Senum, G., Smith, S., Wang, J., Watson, T. B., and Springston, S. R.: Atmospheric Radiation Measurement (ARM) Aerosol Observing Systems (AOS) for Surface-Based In Situ Atmospheric Aerosol and Trace Gas Measurements, J. Atmos. Ocean. Technol., 36, 2429–2447, https://doi.org/10.1175/JTECH-D-19-0077.1, 2019.
- van den Heever, S. C., Marinescu, P. J., Heikenfeld, M., White, B. A., Fridlind, A. M., Stier, P., Saleeby, S. M., Andreae, M. O., Barretth, A. I., Barthlott, C., Cherian, R., Fank, J., Hoose, C., Jensenl, M. P., Matsui, T., Miltenberger, A. K., Quaas, J., Rosenfeld, D., Shpund, J., Vie, B., and Zhang, Y.: A model intercomparison project exploring aerosol impacts on deep convective clouds, manuscript submitted for publication, 2025.
- Varble, A. C., Igel, A. L., Morrison, H., Grabowski, W. W., and Lebo, Z. J.: Opinion: A critical evaluation of the evidence for aerosol invigoration of deep convection, Atmos. Chem. Phys., 23, 13791–13808, https://doi.org/10.5194/acp-23-13791-2023, 2023.
  - Wang, D., Jensen, M. P., Taylor, D., Kowalski, G., Hogan, M., Wittemann, B. M., Rakotoarivony, A., Giangrande, S. E., and Park, J. M.: Linking Synoptic Patterns to Cloud Properties and Local Circulations Over Southeastern Texas, J. Geophys. Res., 127, e2021JD035920, https://doi.org/10.1029/2021JD035920, 2022.
- Wang, D., Kobrosly, R., Zhang, T., Subba, T., van den Heever, S., Gupta, S., and Jensen, M.: Aerosol impacts on isolated deep convection:
  findings from TRACER, Atmos. Chem. Phys., 25, 9295–9314, https://doi.org/10.5194/acp-25-9295-2025, 2025.
  - Xue, H. and Feingold, G.: Large-Eddy Simulations of Trade Wind Cumuli: Investigation of Aerosol Indirect Effects, J. Atmos. Sci., 63, 1605–1622, https://doi.org/10.1175/JAS3706.1, 2006.
- Yang, Z.-L., Niu, G.-Y., Mitchell, K. E., Chen, F., Ek, M. B., Barlage, M., Longuevergne, L., Manning, K., Niyogi, D., Tewari, M., and Xia, Y.: The community Noah land surface model with multiparameterization options (Noah-MP): 2. Evaluation over global river basins, J. Geophys. Res., 116, https://doi.org/10.1029/2010JD015140, 2011.





- Yano, J.-I.: Basic convective element: bubble or plume? A historical review, Atmos. Chem. Phys., 14, 7019–7030, https://doi.org/10.5194/acp-14-7019-2014, 2014.
- Yin, J., Pan, Z., Mao, F., Rosenfeld, D., Zang, L., Chen, J., and Gong, J.: Large effects of fine and coarse aerosols on tropical deep convective systems throughout their lifecycle, npj Clim Atmos Sci, 7, https://doi.org/10.1038/s41612-024-00739-6, 2024.
- Öktem, R., Romps, D. M., and Varble, A. C.: No Warm-Phase Invigoration of Convection Detected during GoAmazon, J. Atmos. Sci., 80, 2345–2364, https://doi.org/10.1175/JAS-D-22-0241.1, 2023.